Oil & Natural Gas Technology

DOE Award No.: DE-NT0005668

Quarterly Report

October 2009 to April 2011

Gas Hydrate Characterization in the GoM using Marine EM Methods

Submitted by:
Scripps Institution of Oceanography
University of California San Diego
La Jolla, CA 92093-0225

Principal Investigator: Steven Constable

Prepared for:
United States Department of Energy
National Energy Technology Laboratory

May 2, 2011

Office of Fossil Energy

TABLE OF CONTENTS

LIST OF FIGURES

LIST OF TABLES

EXECUTIVE SUMMARY All Milestones for Phase 2 of this project have been met. A six month extension was granted to complete the laboratory electrical conductivity measurements on gas hydrate, which was originally scheduled for Phase 1.

Preliminary apparent resistivity pseudosections of the CSEM data where generated at the end of Phase 1, and these results were presented at the 2009 Fall AGU meeting. Since then the CSEM processing codes have been improved to include a more robust error estimation as well as other details (such as including transmitter current as it varies with time, rather then using a constant value, and applying a clock drift correction to all receivers). All data were reprocessed using this new processing code (see Myer et al., 2010). In addition, we generated a unique electric field amplifier calibration for each receiver (Wheelock, pers. comm.).

The Vulcan (our towed fixed-offset receiver) data have been processed for all survey locations. We found that the AC 818 Vulcan data are not sensitive to seafloor resistivity variations, probably because of the higher tow altitude (90m) used here - we were still experimenting with the trim of Vulcan. We lowered the tow altitude considerably (to 65 m) at MC 118, and this improved EM coupling with the seafloor. Vulcan pseudosections were produced for the MC 118 survey, and the results show a resistive area at the SE crater, in conductive surrounding sediments. This is the most significant result to date of the CSEM field data as it pertains to hydrate. At other survey areas we are able to map geologic structures, such as water saturated channel sands and salt, but much more rigorous analysis (2D or even 3D) is needed before we can tease out resistive anomalies due to hydrate in the presence of the more complex bathymetry and structures.

Preliminary pseudosections were presented at the NETL/DOE meeting in Atlanta, Georgia in late January 2010 for all surveys (AC 818, GC 955, WR 313, MC 118). In late February we submitted a *Fire in the Ice* article about the MC 118 Vulcan pseudosections, which was subsequently published. In late March/early April, 2010 we distributed the processed CSEM data with version 1.0 of the navigational parameters for the transmitter and version 2.0 of the receiver positions to the sponsors (an update was made to include the offset of the hull transducer from the GPS antenna). At this time we also had a final schematic and all necessary parts to build a hydrate conductivity cell which allows us to form hydrate in-situ. We submitted: (1) a *First Break* article about preliminary results from GC 955 and MC 118, which was later published in June, 2010; and (2) an Abstract to the 20th EM Induction Workshop, Giza, Egypt. A poster about the GoM CSEM data was later presented at this meeting in September 2010. During 2010 we revisited the development of an OCCAM total field navigation (TFN) program to solve for the transmitter's navigational parameters. Work on the OCCAM TFN program continued throughout the remainder of Phase 2.

In June and July of 2010 initial ice tests were made in the conductivity cell and in August of 2010 the cell was shipped to Menlo Park. At Menlo Park hydrate was made within the cell and cryo-SEM images of the hydrate were produced later in the fall. Wyatt DuFrane, a post-doctoral scholar at LLNL, joined the project in the fall of 2010 and made two runs of electrical conductivity measurements on pure hydrate. A meeting was held at the USGS Menlo Park facility in January of 2011 to discuss the conductivity cell results and start preparing a paper for publication in *Geophysical Research Letters* . This paper has now been accepted for publication. We also planned future runs for the cell with sediment-hydrate mixtures which were recently completed (April 2011). In Jan/Feb 2011, an abstract about the Vulcan CSEM field data was submitted for presentation at the MARELEC 2011 meeting, the 7th International Marine Electromagnetics conference, held in La Jolla, CA., June 2011.

We held our annual sponsor's meeting in March, 2011 and presented the Hydrate Ridge work, the Gulf of Mexico work, and the laboratory work. Two conference papers were written and accepted for a poster and oral presentation at the 7th International Conference on Gas Hydrates that will be held in Edinburgh in July 2011. The OCCAM TFN program has been run for all surveys. New ocean bottom electromagnetic receiver (OBEM) pseudosections were generated for MC 118 using the new transmitter geometry, with significantly improved agreement at crossing tow lines. The new pseudosections were used to compute hydrate volumes using both Archie's Law and the Haskin-Strikmen bounds. MC 118 has relatively flat

bathymetry in comparison to WR 313 , GC 955 and AC 818, making it amenable to 1D inversion. The 1D interpretations show sensitivity to a depth of 2 km, but the results have not proved to be particularly useful. 2D forward model meshes have been prepared so that 2D forward models can be implemented for each CSEM tow line at all survey locations.

References: David Myer, Steven Constable and Kerry Key, 2010, Broad-band waveforms and robust processing for marine CSEM surveys. Geophys. J. Int. (2010) doi: 10.1111/j.1365-246X.2010.04887.x

PROGRESS, RESULTS, AND DISCUSSION

Phase 1. Task 1.0: Project Management Plan. Done.

Task 2.0: Technology Status Assessment. Done.

Task 3.0: Collect Marine CSEM Field Data. Done.

Task 4.0: Preliminary Field Data Interpretation. Originally Task 5. Done.

Phase 2. Task 5.0: Design and Build Conductivity Cell. Originally Task 4. Done.

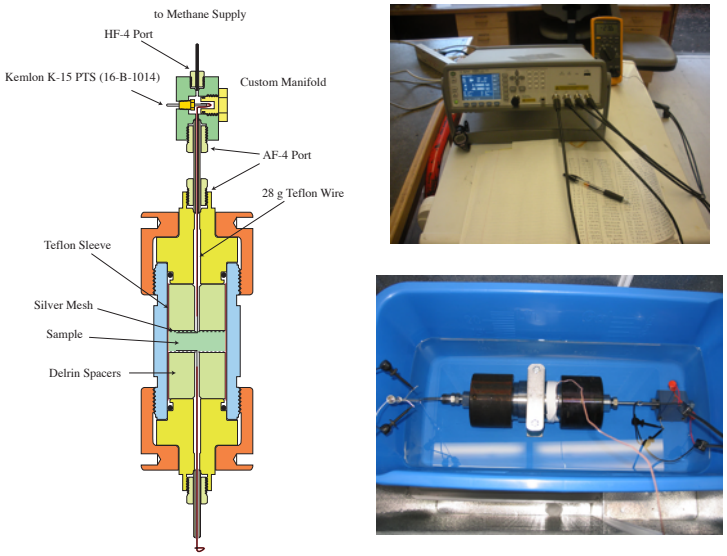

Figure 1: Schematic of the conductivity cell (left), and original Scripps setup for calibration runs on ice. Right top is the Agilent E4980 Precision LCR meter and right bottom is the cell sitting in a propylene glycol bath within a chest freezer.

We designed a specialty pressure cell to form polycrystalline CH_4 hydrate for impedance (Z) measurements (Figure 1 left and Figure 4A). The cell is built around a commercially available double-ended pressure vessel manufactured by High Pressure Equipment Co. with a pressure rating of 5,000 psi (34.5 MPa). Silver foil electrodes are connected by Teflon insulated wire to high pressure electrical feedthroughs (Kemlon brand K-15) on the inner (high pressure) side and an Agilent E4980A LCR (inductance-capacitance-resistance) meter on the outer side. The cell encloses a 5 x 1.25-cm disc shaped sample, with electrodes at each end and capped by Teflon spacers surrounded by a Teflon sleeve. The Agilent LCR meter was used to measure complex Z spectra between 20 Hz to 2 MHz with a relative accuracy 0.01% degrading to 1% for Z of 10

MΩ. The assembly was tested for electrical leakage using a blank sample made of Teflon, ice frozen from reagent grade water, and a variety of parallel resistor-capacitor (R-C) circuits (10-316 kΩ; 1.15-22 pF).

Figure 1 (bottom right) shows the experiment set up for the ice calibrations runs carried out at Scripps. The conductivity cell sits in a propylene glycol bath within a chest freezer with electrical connectors for the LCR meter. Figure 1 (top right) shows the set up for the Agilent E4980A Precision LCR meter and Fluke multimeter (for reading a thermistor in the glycol bath).

For ice calibration runs we used HPLC (high performance liquid chromatography) reagent grade water (maximum of 1 ppm contaminants), outgassed it under a vacuum for an hour, and froze it slowly (over 10-20 hours) in a teflon sleeve. We filed off the meniscus with a steel file. We loaded the ice puck (about a 1/2 inch height by 2 inch diameter) into the cell with two disks of silver foil as electrodes. These are blocking electrodes, since they are polarizing and don't allow transfer of charge, but they work at high frequencies and there are extensive data in the literature for comparison.

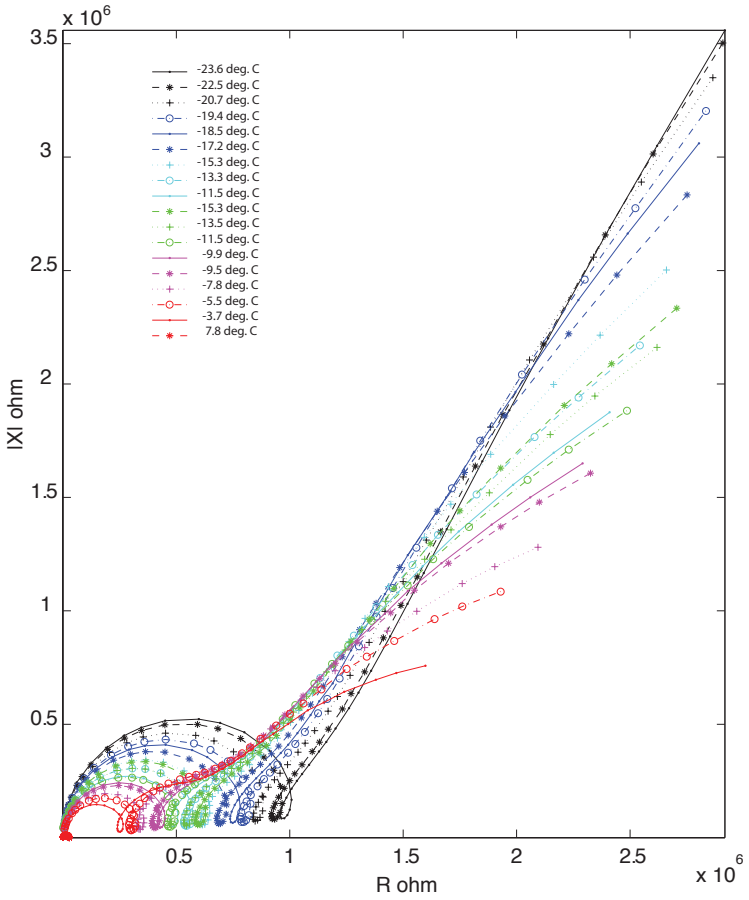

Figure 2: Cole-Cole plots of the calibations runs on ice at varying temperatures.

The Agilent LCR meter was used to make resistance (R, real component) and reactance (X, imaginary component) measurements over a frequency range of 20 Hz to 2 MHz using an applied voltage of 1 V (2 V was also used, and gave similar results). These measurements were repeated at different temperatures and Cole-Cole plots are shown in Figure 2. There are three main features present in all of the measurements below 0^oC:

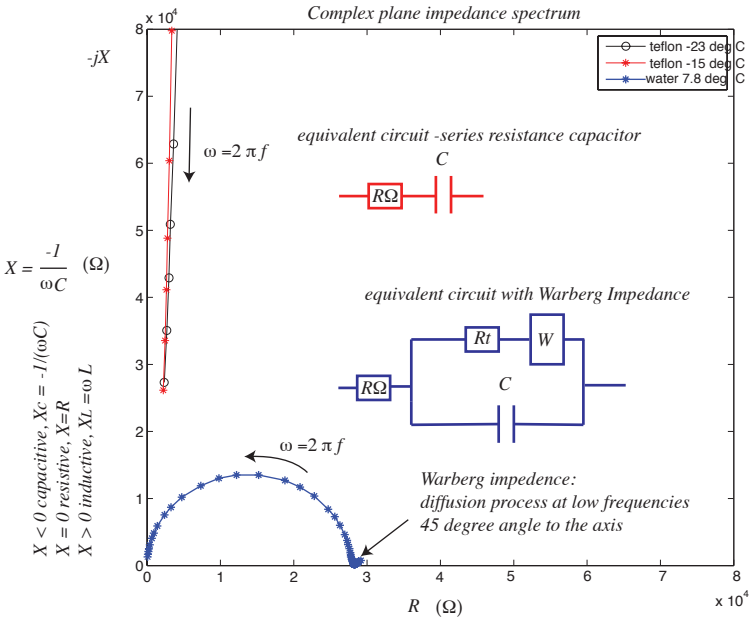

Figure 3: Calibration runs on teflon disc at -23^oC, -15^oC (red, black), and confined water (blue). An equivalent circuit model has been labeled for the teflon as a series resistance capacitor and for the water as an equivalent circuit (series resistor with a parallel resistance capacitor) with a Warberg Impedence. Equivalent circuit sketched is from Cogger and Evans (1999). Note that only a few frequencies are plotted for the teflon disc (600 Hz to 2 MHz).

(1) The high frequency portion that is a well-formed semi-circle is presumably from Debye relaxation and almost certainly contains the system capacitance. This can be determined by CNLS (complex nonlinear least square) equivalent circuit fitting of the data. The peak of the circle also gives the Debye relaxation time, which for pure ice at -10^oC is around 5x10^{-5} s.

(2) The low frequency portion looks like a Warburg impedance response and is expected for this set-up (Jeff Roberts, pers. comm.).

(3) The curly-cue on the low frequency side of the semi-circle is often interpreted as dissolution, corrosion, or thin-film response (Jeff Roberts, pers. comm.).

We allowed the ice to melt and made a measurement on the confined water, and have also tested the cell with a Teflon disc as a sample to estimate the system response. Figure 3 shows the teflon disk runs and the water runs with a sketch of an equivalent circuit model for each case.

References:

Cogger, N.D. and N.J. Evans. 1999. An Introduction to Electrochemical Impedence Measurements. Technical Report No. 6 Part No. BTR006. Solartron Limited.

Petrenko V.F. and R.W. Whitworth. [2006] Physics of Ice. Oxford University Press Inc. , New York.

Task 6.0: Make Hydrate and Hydrate/Sediment Conductivity Measurement.

After the ice runs showed that the cell was operating correctly, we moved it to the USGS lab at Menlo Park, where the work was carried out primarily by Wyatt DuFrane and Laura Stern. We performed 4 runs

with CH_4 hydrate: run 1 with a thermocouple installed in the cell to verify the synthesis process and extent of reaction, runs 2 and 3 to measure σ of pure methane hydrate and, run 4 to synthesize a uniform phase distribution of a methane hydrate + sand sample. Samples of CH_4 hydrate were synthesized from a granular ice + CH_4 gas mixture at 25 $\pm$5 MPa using a temperature cycling method described in Stern et al. (1996; 2004). The pressure vessel sits in a D-limonene temperature bath above a heater, both in a chest freezer maintained at $\approx$ -15°C (Figure 1B and 1C). The reactant ice was made from a block of nearly gas-free ice grown from distilled-deionized (DDI) water, then crushed and sieved to 180-250 μm.

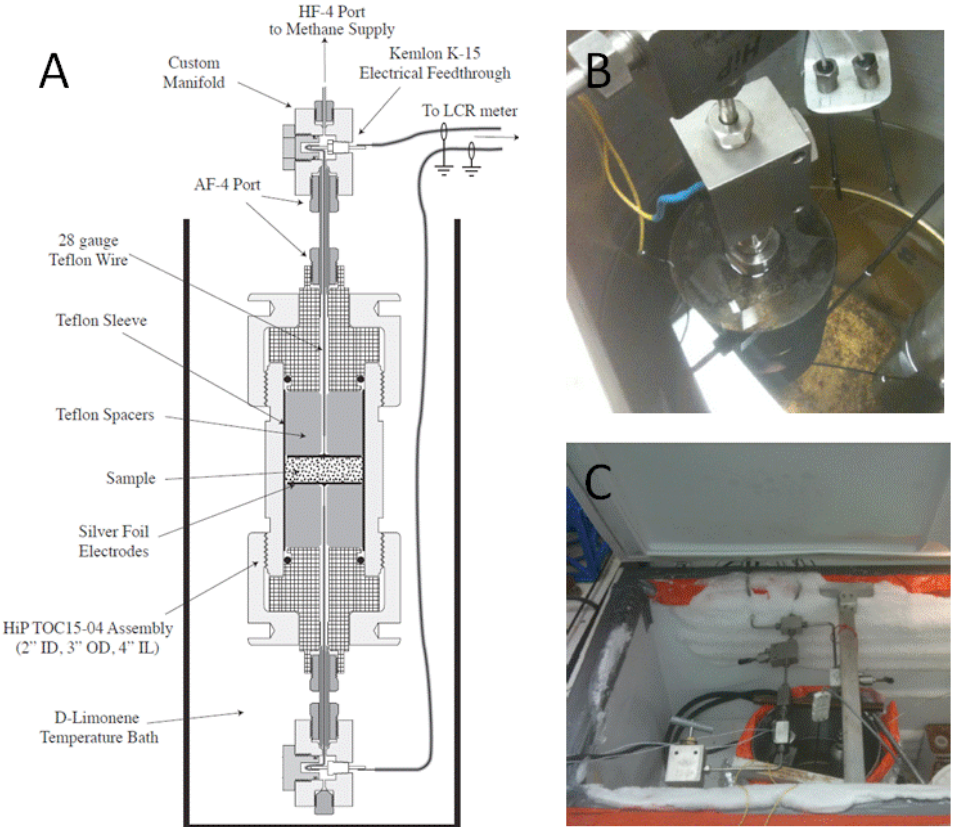

Figure 4: A) Schematic of pressure cell for CH_4 hydrate synthesis and σ measurement (from Du Frane et al., in press, Geophys. Res. Lett.). B) Pressure cell inside a D-limonene temperature bath, with CH_4 line. C) D-limonene temperature bath and pressure plumbing above heater inside a chest freezer.

Run 1: hydrate synthesis with thermocouple and cryoSEM images

Cryogenic scanning electron microscopy (cryo-SEM) was used to observe the grain size and appearance of the final CH_4 hydrate formed in run 1. For this procedure the vessel was cooled sufficiently with liquid nitrogen prior to depressurization and opening of the cell. A thermocouple embedded in the sample was used to ensure stability of the hydrate during the quenching procedure, recovery, and transfer to the cryo-preparation station (Gatan Alto Model 2100). The sample was cleaved under vacuum in the preparation station to produce fresh surfaces uncontaminated by water condensation, and then transferred under vacuum to a LEO982 field emission SEM. A thermocouple embedded in the SEM sample stage monitored temperature throughout the imaging process. Imaging was conducted at temperature < - 185 C, vacuum < 10^{-6} kPa, and accelerating voltage of 2 kV. Further details are given in Stern et al. (2004).

For the first hydrate synthesis the starting ice grains were packed tighter than normal to reduce porosity, and

the sample ended up taking longer to fully synthesize than normal (a couple of weeks). A thermocouple was in the sample so we could gauge when hydrate formed. The results appear excellent (Figures 5-11). Grains are coarser than usually produced, probably because the sample cycled to high temperature so many times. It is also less porous than usual; the overall sample porosity is about 20%, instead of the usual 30%.

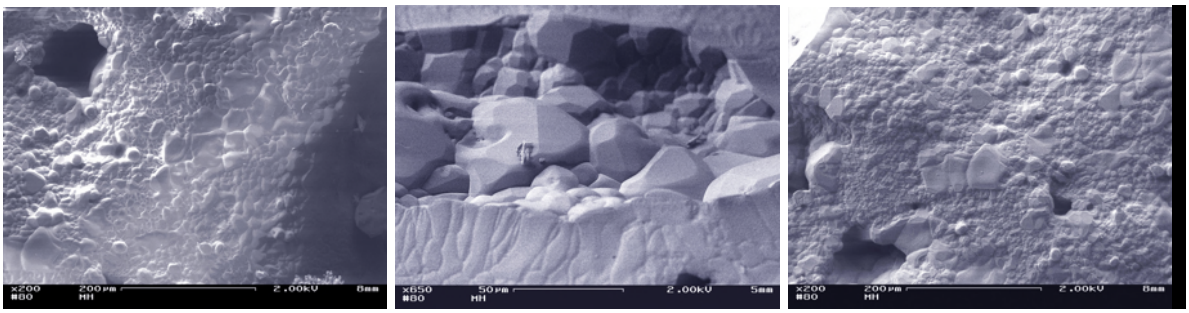

Figure 5: Cryogenic scanning electron microscopy images of pure methane hydrate formed in the electrical resistivity cell. The resulting polycrystalline material has 20-70 μm average grain size and 20% intergranular porosity (middle).

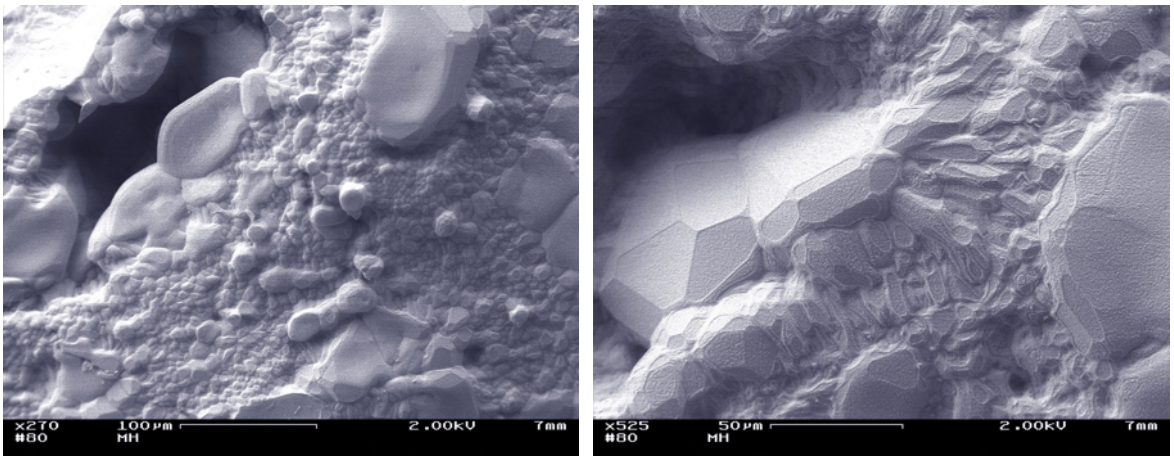

Figure 6: Higher magnification of Figure 1. Grains are still very easy to distinguish.

Figures 5 to 11 are cryogenic scanning electron microscopy (SEM) images for this first sample of hydrate in the cell. The grains typically range from 15 to 60 microns, which is similar to what is seen in gas hydrate from nature. Many grains here look smaller due to the small portion of the grain that is exposed. Some of the photos in Figures 1 to 7 show fresh fracture surfaces through grains, while others expose cavities where you can see well formed crystals. The grain size is consistent throughout. Individual grains are fully dense as can be seen in the first several photos. Sublimation and surface deterioration gives the hydrate a nano-or meso- porous appearance. Numerous photos are shown here to help illustrate that process. The spongy appearance is merely an artifact of the high-vacuum conditions in the SEM chamber, and is not a property of the original material.

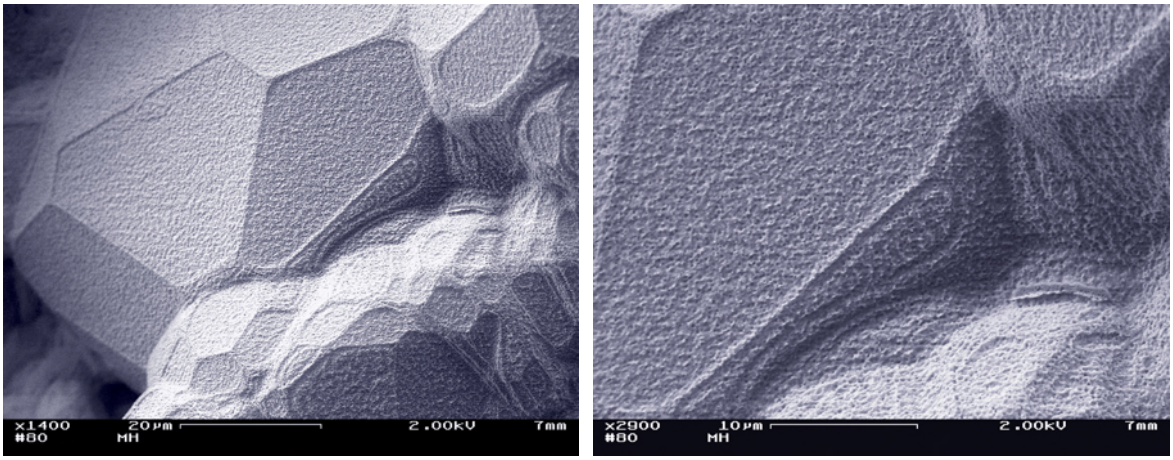

Figure 7: Two close-ups that show a nano-porous appearance.

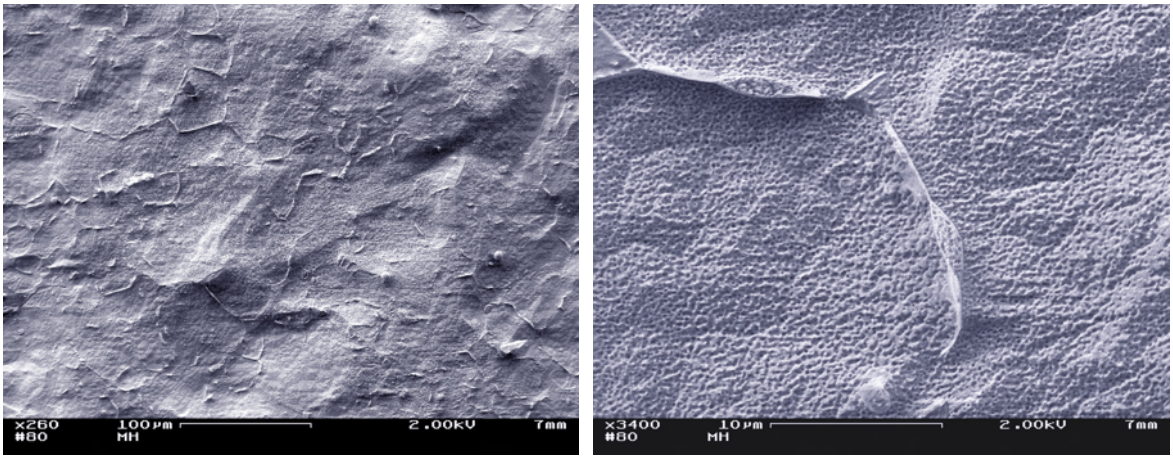

Figure 8: Grain boundaries in a dense section of hydrate. Original and smaller sub-grains are developing into coarser grains (left). A close up is shown on the right.

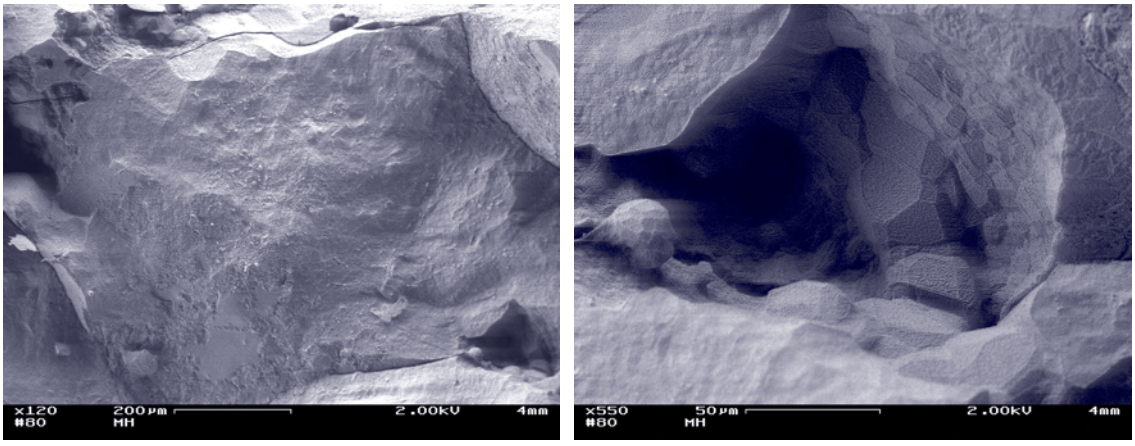

Figure 9: Low-magnification overview showing overall density of the sample (left). Detail of lower right cavity (right).

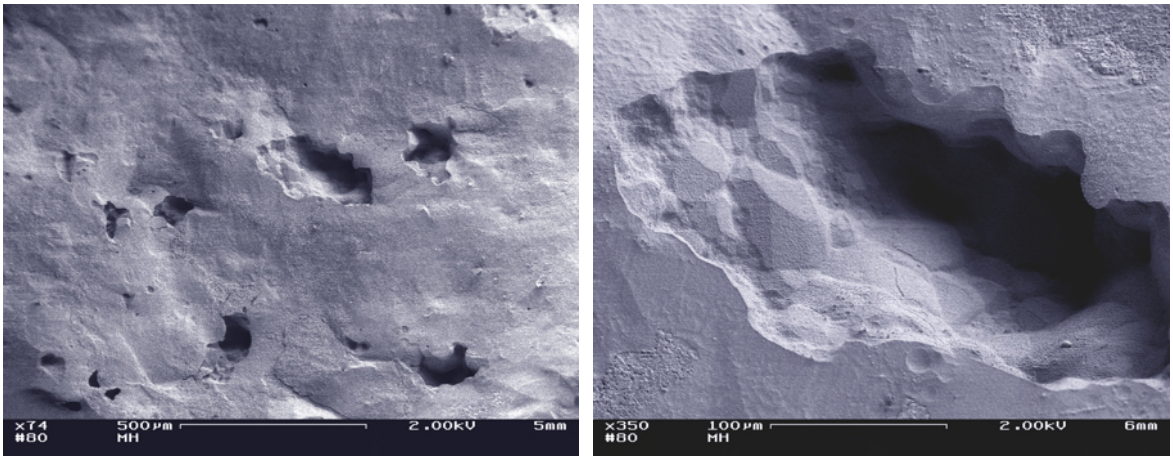

Figure 10: Another low-magnification overview showing overall sample texture (left). Detail of cavity in mid-portion of previous photo (right)

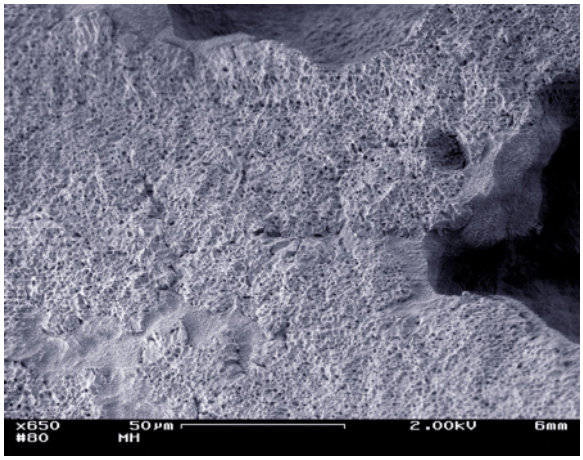

Figure 11: Very late stage surface deterioration.

Run 2-3: hydrate synthesis with electrodes and activation energy estimates

We measured Z and σ in runs 2 and 3 during the first heating cycle, after full reaction to CH_4 hydrate, and after samples were dissociated back into polycrystalline ice. Heating was isochoric such that the pore pressure of CH_4 gas increased during the measurement. While heating or cooling, temperature in the center of the run 1 sample lagged slightly behind bath temperature by 1-5°C, leading to slight uncertainty in sample temperature during heating for runs 2 and 3. We addressed this in run 3 by monitoring Z at a single frequency after each heating increment and recording σ after it stopped changing; we called this 'step-dwell'.

Figure 12 is a Cole-Cole plot of the imaginary part of impedance, $|X|$, versus the real part, $|R|$ of polycrystalline methane hydrate from runs 2 and 3 at 4^oC. The impedance spectra are modeled by taking the impedance magntiude, $|Z| = (R^2 + X^2)^{1/2}$, corresponding to the highest value of the impedance phase, $\theta = tan^{-1}(X/R)$. This corresponds to the length of the arc on the real axis in the Cole-Cole plot. The Z spectra were modeled with two parallel resistor-capacitor pairs in series. Fitting results are given in the upper-left inset of Figure 12, with errors provided in parentheses. The lower resistance arc that dominates the high frequency portion of the spectra is a material property of the sample (R1, C1), and the larger resistance arc that dominates the low frequency portion of the spectra is caused by electrode polarization (R2, C2). The resistivity is computed by multiplying the resistance, R, by a geometric factor of 0.16m,

which is the area of the measurement surface (average electrode area =$\pi(0.0254\text{m})^2$) divided by the sample thickness (0.0127m). $R2$ is not well determined.

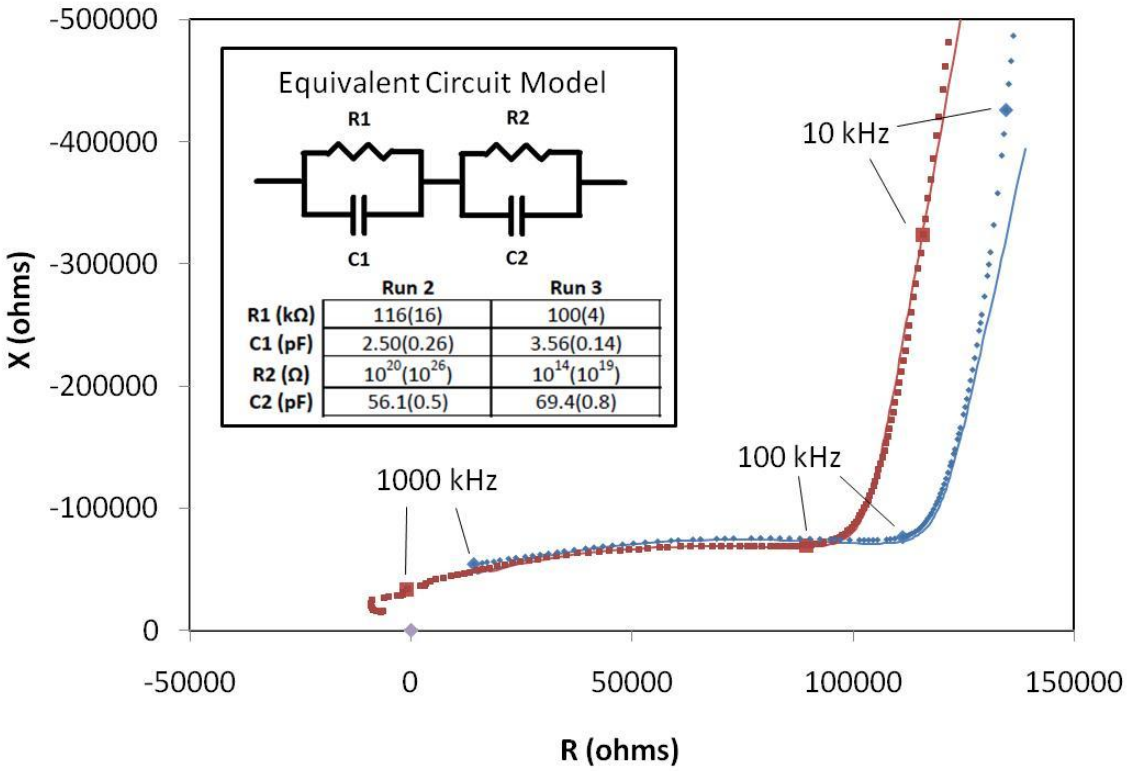

Figure 12: A Cole-Cole plot is shown for the hydrate sample from run 2 and 3 and in the top corner is an equivalent circuit model.

For runs 2 and 3, σ was measured during the initial heating cycle and after CH_4 hydrate was fully synthesized (i.e. after > 6 heating cycles). The samples were then dissociated to polycrystalline ice by venting the pressurized CH_4 from the sample at -15° C (1 day for run 2, and 13 days for run 3). The σ of the samples increased during dissociation to ice (Figure 13). In both runs, σ of the samples as CH_4 hydrate were a factor of 3-4 lower than σ of the samples as ice. For both ice and CH_4 hydrate σ exhibited typical Arrhenius behavior (Figure 13). We thus fit the σ data as a function of absolute temperature (T) using $\sigma(T) = \sigma_o e^{-E_a/RT}$ where σ_o is a pre-exponential constant corresponding to T = ∞, R is the gas constant, and E_a is the activation energy. The slope of Figure 13 is proportional to the activation energy. Larger error is associated with E_a calculated during active heating because of the variable amount by which the bath temperature lagged sample temperature. We consider the E_a calculated from run 3 using the 'step-dwell' approach to be the more reliable, nevertheless there is good agreement between runs 2 and 3 (Figure 13). Table 1 lists the constants for runs 2 and 3 of the Arrhenius relationship.

Table 1: Arrhenius constants for hydrate

constant	run 2	run 3
E_a (kJ/mol)	27.9	30.6
Log(σ_o (S/m))	0.965	1.50

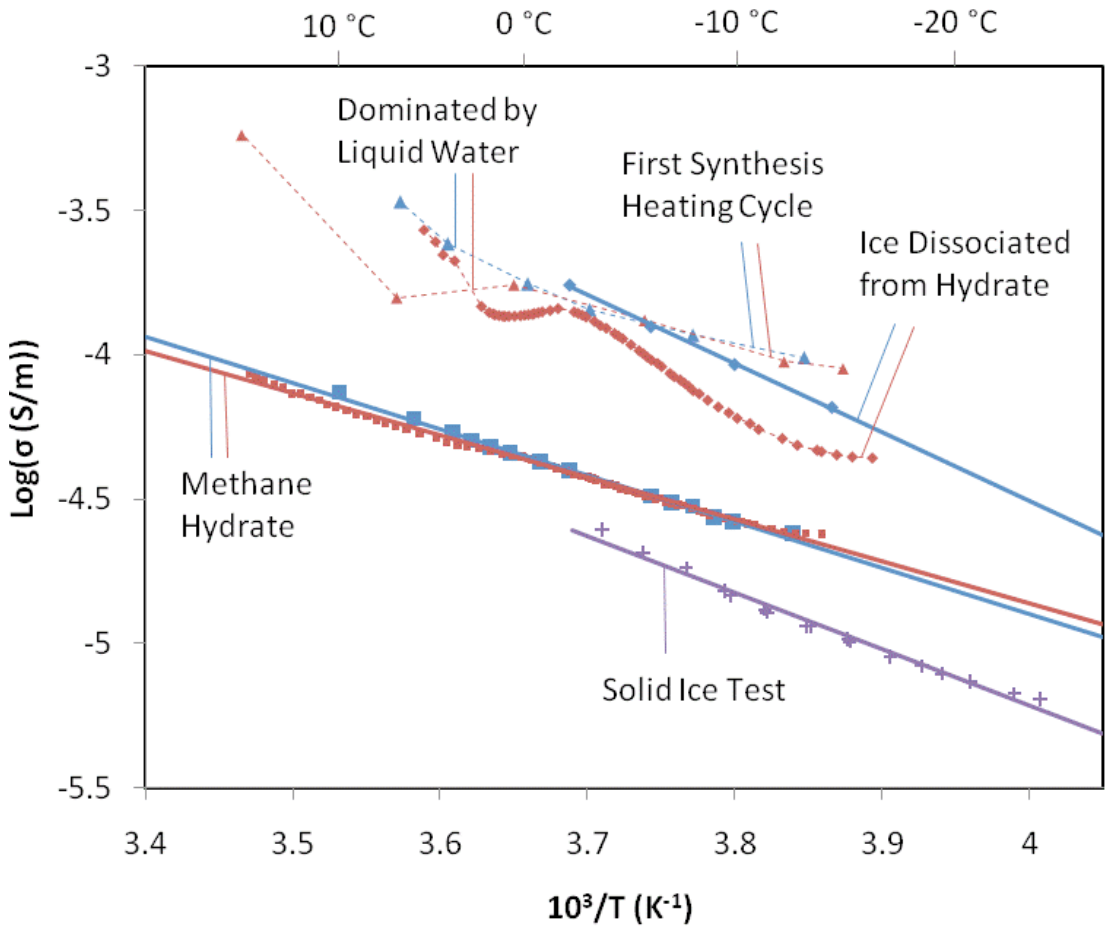

Figure 13: The σ data collected during the first heating cycle (triangles), after methane hydrate synthesis (squares), and after dissociation to ice (diamonds), showing the reproducible measurements of runs 2 (red) and 3 (blue); and solid ice frozen from reagent grade water (purple plus signs). Data fits are shown as solid lines (corresponding colors). Samples as CH_4 hydrate are 0.5-0.6 log units below values as ice. E_a is 33% lower for CH_4 hydrate than ice (proportional to the slope of data fits, results in Table 1). Measurements during the first heating cycle after crossing the ice point remain relatively high due to the small amount of unreacted H_2O in grain interiors prior to full reaction to hydrate (modified from Du Frane et al., in press, Geophys. Res. Lett.).

Run 4: hydrate-sediment mixture cryoSEM images

Natural occurrences of gas hydrates comprise of mixtures with sediment and ice or seawater. The σ that we measure for gas hydrate is much less than for seawater (.56 to 38 S/m for salinities between 5 and 40g/L, at 5°C) (CRC Handbook of Chemistry and Physics) and much greater than quartz sand ($< 10^{-18}$ S/m) (Serway, 1998). Connectivity of multiphase assemblages is an important factor in determining the σ of mixtures. The presence of a well connected seawater phase would dominate the properties of the mixture, consistent with higher σ measurements of samples mixed with water (10^{-3}-10^{-2} S/m) in comparison to our σ measurements of unmixed CH_4 hydrate (Spangenberg and Kulenkampff (2006); Lee et al., 2010; Ren et al., 2010). Conversely, high saturations of gas hydrate would dominate mixtures that have little or poorly connected water present; further work is especially needed to resolve mixing relationships for this case. Another potentially important factor in determining the σ of gas hydrate-sediment mixtures is chemical interaction between phases. The presence of fine grained clays and minerals may increase ionic impurities

within the gas hydrate phase, which would likely alter the electrical properties of the gas hydrate and overall mixture.

A cryo-SEM image of a sediment-hydrate mixture formed within the cell is shown in Figure 14. Analysis of the σ data from this run is ongoing.

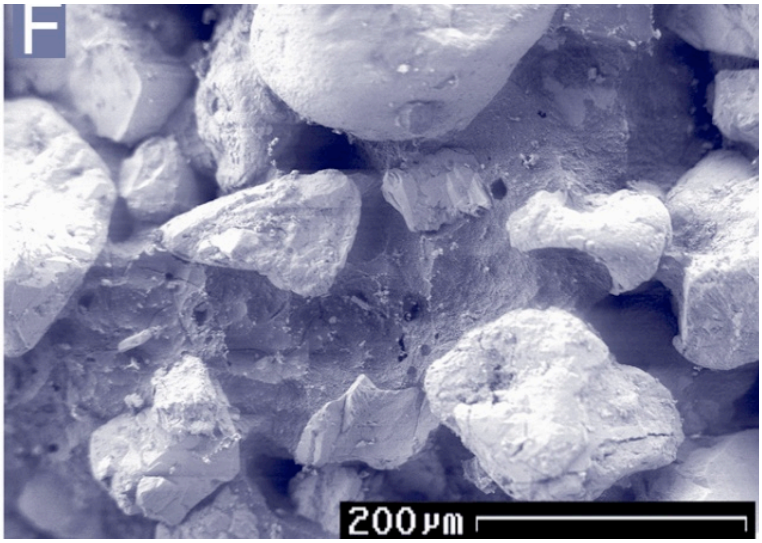

Figure 14: Cryo-SEM images of samples formed in run 4 at varying magnifications Image F shows the run 4 sample, in which CH_4 hydrate (appears as the darker-colored connecting material between the sand grains) and OK#1 quartz sand grains (appear light in color and stand high in relief due to partial sublimation of the CH_4 hydrate) each occupy 50 vol. % of the solid material here.

References

CRC Handbook of Chemistry and Physics.

Lee JY, Santamarina JC, and Ruppel C. 2010. Parametric study of the physical properties of hydrate-bearing sand, silt, and clay sediments: 1. Electromagnetic properties. J. Geophys. Res.;115:B11104, doi:10.1029/2009JB006669.

Ren SR, Liu Y, and Zhang W., 2010. Acoustic velocity and electrical resistance of hydrate bearing sediments. J. Petrol. Sci. and Engineer. 70:52-56.

Serway RA. 1998. Principles of Physics. 2nd Ed. Fort Worth, Texas; London: Saunders College Pub. p. 602.

Spangenberg E, and Kulenkampff J. 2006. Influence of methane hydrate content on electrical sediment properties. Geophys. Res. Lett. ;33(24).

Stern, L. A., S. H. Kirby, and W. B. Durham. 1996, Peculiarities of methane clathrate hydrate formation and solid-state deformation, including possible superheating of water ice, Science, 273(5283), 1843-1848.

Stern, L. A., S. H. Kirby, S. Circone, and W. B. Durham. 2004, Scanning electron microscopy investigations of laboratory-grown gas clathrate hydrates formed from melting ice, and comparison to natural hydrates, Am. Mineral., 89(8-9), 1162-1175.

Task 7.0: Modeling and Inversion of Field Data.

1. Transmitter Navigation

Preliminary apparent resistivity pseudosections of the CSEM data were generated at the end of Phase 1, and the majority of this past year has been spent on improving the navigational parameters for the deep-towed transmitter. The navigational parameters have been estimated in three ways. (1) Initially assuming the transmitter follows directly behind the ship at a distance determine by the wire out and depth of the transmitter. This has almost no information about the crossline position or azimuth of the transmitter antenna. (2) Using a Marquardt total field navigation (TFN) program that uses the close range EM field at seafloor instruments to derive the geometry of the transmitter. This program solves for transmitter X,Y, azimuth and seafloor resistivity at each transmitter position. The weakness with this approach is that the program can be unstable, and requires careful selection of starting parameters to get a solution to converge. Solutions are independent for each transmitter position, and can be very erradic, requiring smoothing of the final models. (3) An OCCAM total field navigation solution was implemented and regularizes neighboring points to eliminate erradic changes in transmitter positions. To date only the MC 118 survey has been analyzed using the new transmitter geometry from the OCCAM TFN program. All other surveys, AC 818, WR 313, and GC 955, are analyzed with transmitter positions from the Marquardt TFN program.

2. Building Apparent Resistivity Pseudosections

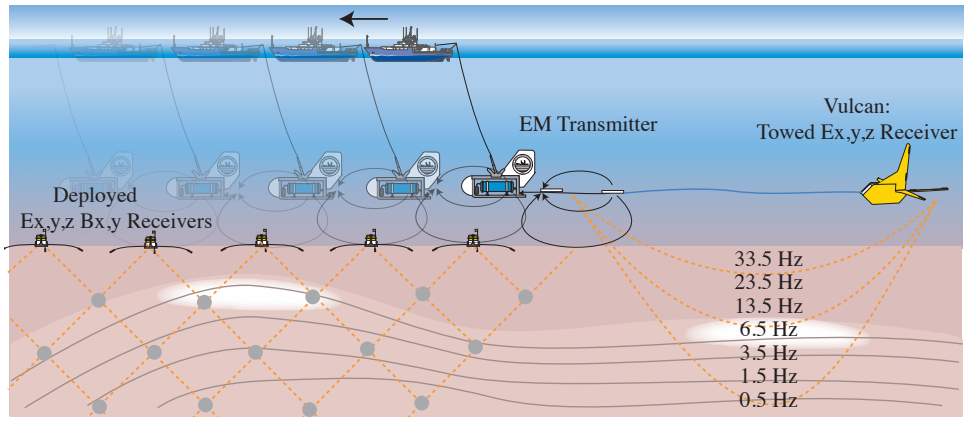

Figure 15: Marine CSEM system showing deployed OBEM instruments and the towed 3-axis electric field receiver called Vulcan. We can build apparent resistivity pseudosections two different ways: The left side shows apparent resistivities derived from OBEM instruments projected to a mid-point between the EM transmitter and receiver, at a pseudo-depth proportional to the transmitter-receiver offset. For the fixed-offset towed receiver (right), apparent resistivities from different frequencies can be projected at the common mid-point based on skin depth, with lower frequencies having larger skin depths/deeper penetration.

The transmitter and receiver geometry was used to generate 1D half-space forward models for various resistivities using the Dipole1D code of Key (2009). The major axis of the data polarization ellipse was compared to the half-space forward models to derive an apparent resistivity for each transmitter-receiver pair. A pseudosection projection technique was used to image the data. Figure 15 (left) shows a schematic of the data projection for mapping ranges into depths; the longer the transmitter-receiver offset the deeper that data point is projected. A similar approach is taken with the Vulcan data except that the Vulcan apparent resistivity pseudosections are generated as a function of frequency. The apparent resistivities are projected into depth using skin depths for each frequency as a length scale, as shown in Figure 15 (right). Pseudosections provide a way to observe lateral variations in resistivity and give qualitative depth relationships. However, they do not provide quantitative depth information, and so the depth scales in the following figures should not be taken literally.

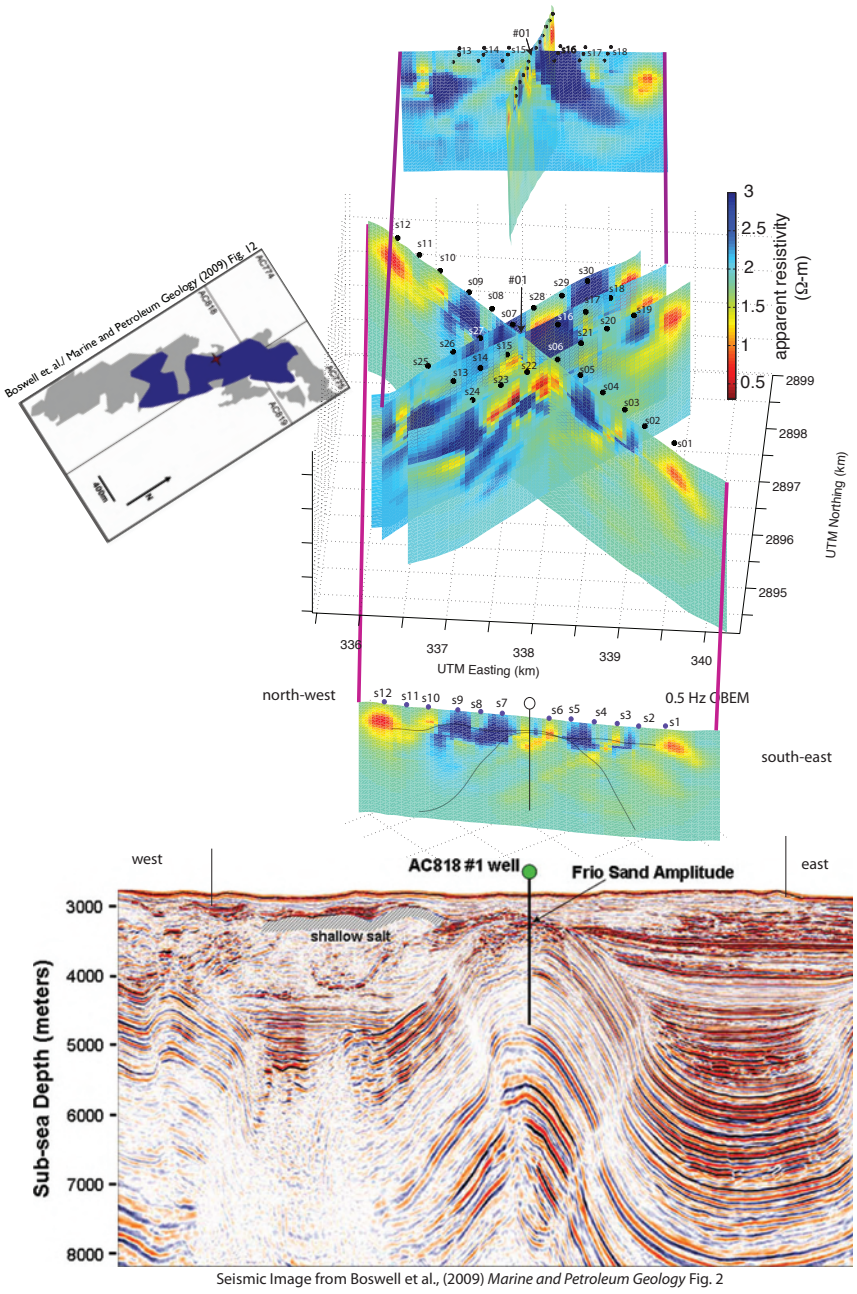

Seismic Image from Boswell et al., (2009) *Marine and Petroleum Geology* Fig. 2

Figure 16: OBEM pseudosection crossplots for AC 818 at a frequency of 0.5 Hz and a closer examination of Line 1 (bottom) and Line 2 (top) with corresponding seismic data. The bottom seismic line is an EW transect showing where the Oligocene Frio sand is above the gas hydrate stability field (labelled as Frio Sand Amplitude) (Boswell et al., 2009b). The left map view shows in blue the gas hydrate distribution within the Frio sand and in grey the water saturated frio sand with low saturations of free gas (Boswell et al., 2009b).

2.1 Alaminos Canyon 818

Chevron encountered a thick (20 m) hydrate-bearing section a few hundred meters below seafloor in an exploration well on this block, with high resistivities (30-40 Ohm.m) evident in the logs. The water depth is around 3,000 m. We deployed 30 receivers and made four transmission tows, centered on the Chevron well (Figure 16). The AC 818 OBEM 0.5 Hz pseudosections are shown in Figure 4 (centre) with a closer

examination of the EW-trending CSEM Line 1 (bottom) and NS-trending Line 2 (top). An EW seismic line and an estimate for gas hydrate distribution in the Frio sand derived from a 3D seismic volume as presented in Boswell et al. (2009b) are included in Figure 16.

All four pseudosections display a consistent image; for example all three NS trending pseudosections have a conductive region to the north-east (NE of sites 30, 18 and 19). The AC 818 pseudosections have a more complex resistivity structure when compared with the MC 118 pseudosections (also true of the WR 313 and GC 955 pseudosections discussed below) and the background resistivity at AC 818 is higher than MC 118, varying from 1.5 to 2 Ω-m. A resistive region trends from the NE to the SW, and is consistent with the map view of the seismic derived hydrate distribution given in Boswell et al. (2009b). The NE to SW OBEM Line 2 pseudosection (Figure 16 top) has a large resistor to the north (site 16) and to the south (site 13 and 14), a pattern of conductive and resistive sediments that could be associated with the pattern of water saturated sand and hydrate-bearing Frio sand (Figure 16 left) given in Boswell et al. (2009b). The NW to SE OBEM Line 1 pseudosection (Figure 16 bottom) has a resistive region (sites 9 and 8) associated with the shallow salt indicated in the seismic section. Seismic bright spots have been documented by Latham et al. (2008) and Hutchinson et al. (2008) and are thought to be associated with free gas. The pseudosections have a resistive region which may correspond to this seismic event (site 7). At the well location itself there is a very subtle resistive region in the shallow section, which could be associated with the LWD resistive region discussed in Smith et al. (2006), but more likely the NE to SW tows are capturing this resistive region. Under sites 5 and 4, a resistive region is present and may be associated with an inferred BSR discussed in Jones et al. (2008). AC 818 is on the Perdido fold 3 (Fiduk et al. 1999) which has pushed the Oligocene Frio sand into the hydrate stability zone (Boswell et al., 2009b, Hutchinson et al., 2008, Jones et al., 2008, Latham et al., 2008). This fold is shown in the EW seismic section and our pseudosections show it to have a background resistivity of 2 Ω-m, attributed to the water saturated Frio sand.

2.2 Green Canyon 955

GC 955 is a prospect in intermediate water depth (1900-2200 m) located seaward of the Sigsbee Escarpment and at the mouth of Green Canyon, which brings sediments onto the deep seafloor. There is surface evidence of features often associated with hydrate, such as mud volcanoes. A surface channel is present in the bathymetry and channel sands are present at depth. One such channel sand was a target of the JIP, and is well defined in seismic data, which shows evidence of gas accumulation near the base of the hydrate stability field (McConnell et al., 2010; Hutchinson et al., 2008; Jones et al., 2008).

We deployed 20 seafloor instruments along two transmission lines as close as possible to the anchor pattern of a drill rig (Figure 17) that was operating on this block during our survey. For this reason the CSEM lines do not intersect directly with the JIP drill locations. The N-S CSEM line is located in an area of four-way closure consisting of a bathymetric high cored by allochthonous salt above which sandy levee sands are sealed by a regional shale layer (Hutchinson et al., 2008). Faults here provide migration pathways for fluids (Hutchinson et al., 2008). This allochthonous salt is a large regional feature that is hour-glass shaped and extends to the south into Walker Ridge (McConnell et al., 2010 and references therein). Seismic horizon C, shaded in grey, is a channel sand expected to contain gas hydrate (Hutchinson et al., 2008), and which may extend to our E-W CSEM line. A horseshoe shaped scarp face also exists to the east, which likely resulted from internal failure due to fluid flow and gravitational forces at over-pressured sand cropping at the base of the Sigsbee escarpment (McConnell et al., 2010 and references therein). A similar process is likely occurring below the E-W line to the east of the area of four-way closure, where there is an amphitheater-shaped region of seep sapping (McConnell et al., 2010).

Pseudosections for the E-W and N-S CSEM tows are shown for the OBEM receivers at the fundamental frequency of 0.5 Hz in Figure 17 (right). One main observation is that the N-S CSEM line is more resistive than the E-W CSEM line. This is likely caused by a regionally extensive N-S trending allochthonous salt body present along this line. The E-W line is perpendicular to this structure and its pseudosection is not dominated by the presence of salt. Gas hydrates were found in GC 955 well ‘H’ and ‘Q’, both targeting

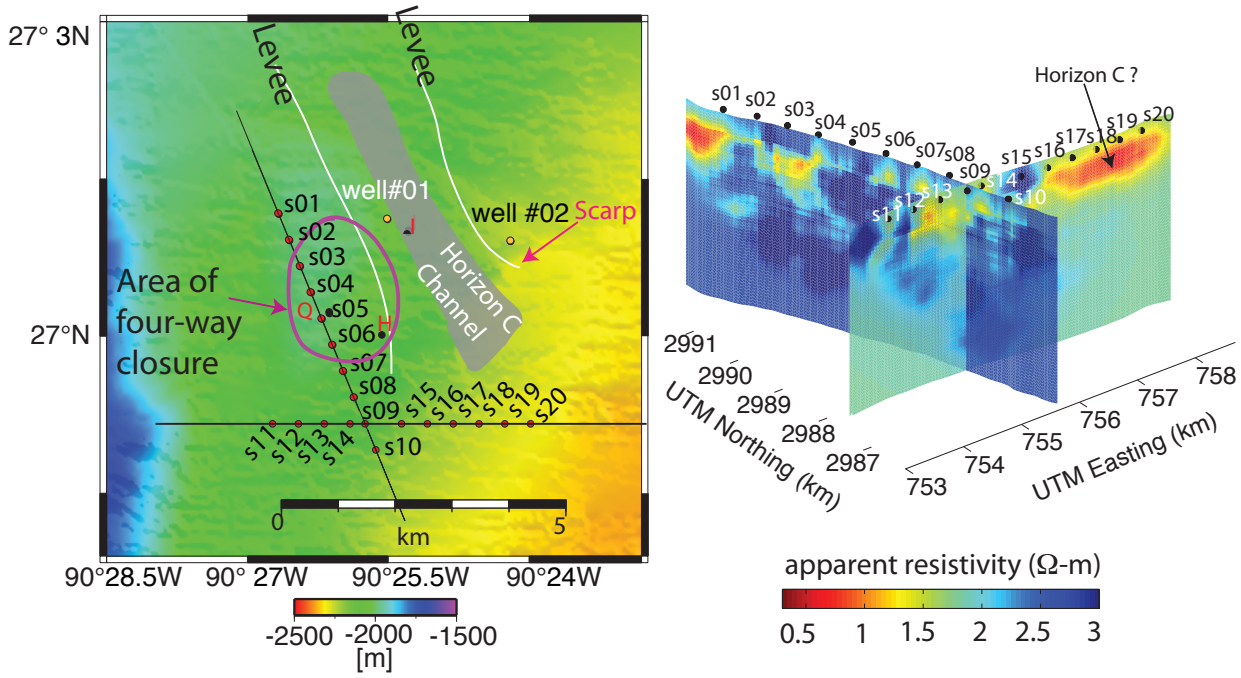

Figure 17: GC 955 survey map with annotations from Hutchinson et al. (2008) (left) and 0.5 Hz OBEM pseudosections (right).

hydrate filled sands that are located in the area of four-way closure (McConnell et al., 2010). In addition, well 'H' also encountered fracture-filled hydrate above the sand target. The drilling at well 'Q' had to be aborted due to gas flow, either caused by hydrate dissociation or free gas (McConnell et al., 2010). The N-S pseudosection is resistive at site s05, consistent with the existence of hydrate in the coincident JIP well 'Q'. The N-S and E-W CSEM lines cross at site, s09 and tie together well.

Figure 18 (left) shows Vulcan and 6.5 Hz and 0.5 Hz OBEM pseudosections for the E-W CSEM line. The three images tell a consistent story: a conductive region to the east (s16 to s20) and more resistive area on the slope of the bathymetry high (s15, s09, s14), grading into an interspersed conductive and resistive region at the actual bathymetric high (s11-s13). The deep resistor in the 0.5 Hz OBEM pseudosection is likely due to the allochthonous salt and the fact that it is barely seen in the 6.5 Hz OBEM pseudosection indicates it is a deep structure. The resistive region below s11 in the OBEM data is observed in the Vulcan data as well, but is offset due to the different projection geometries of Vulcan and OBEM resistivities. JIP well 'H', located on the flank of the area of four-way closure, is about 1 km north of the E-W CSEM line and is roughly between s09 and s15. Drilling at 'H' found a shale section with fracture-filled hydrate which reaches the seabed and then a deeper occurrence of alternating gas hydrate and water pore fill bearing intervals within a single sand reservoir (McConnell et al., 2010). This is consistent with the resistive region between s15 and s14.

Hydrate was expected to be found in well 'I', which was drilled into the axis of the porous sand channel (horizon C), but water saturated sand with very little hydrate or free gas was encountered (McConnell et al., 2010). This channel sand likely extends to the south and is probably expressed as the more conductive region on the east side between s16 and s20.

The NS tow is shown in Figure 18 (right). The 0.5 and 6.5 Hz OBEM data are dominated by the NS allochthonous salt, but the Vulcan data appears to be insensitive to its presence, being much more conductive than the OBEM data and having very little structure in the electrical resistivity variations across the line.

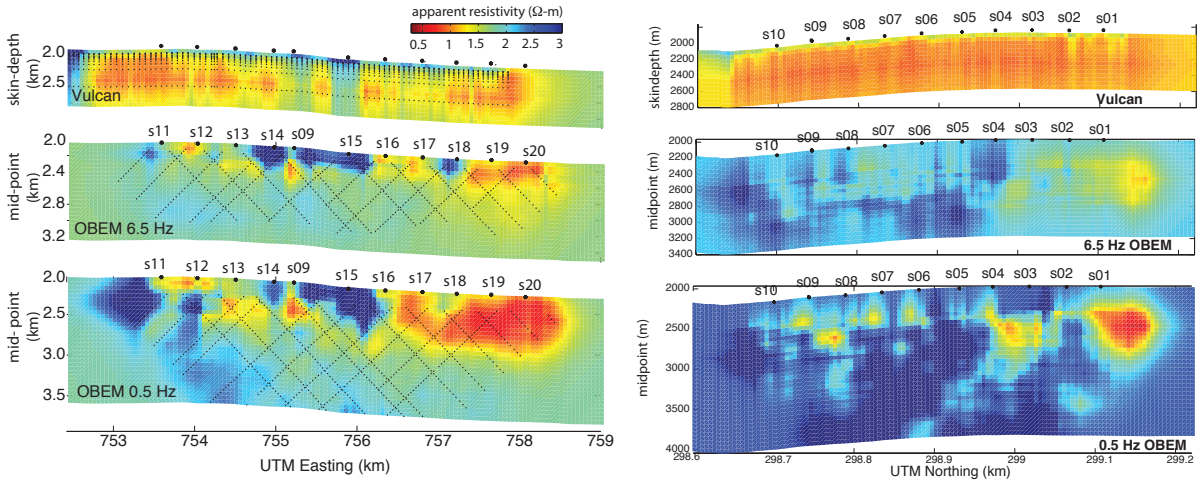

Figure 18: GC 955 EW CSEM line (left) and NS CSEM line (right) for the Vulcan data (top), 6.5 Hz OBEM data (middle) and 0.5 Hz OBEM data (bottom).

Site 5 is roughly at the location of well 'Q' which had little evidence of gas hydrate in the upper mud-rich sediments despite its proximity to well 'H' - which had fracture filled hydrate that reached the seabed (McConnell et al., 2010). In fact evidence for hydrate at 'Q' did not occur until about 430 mbsf in a tight section of the well log, where at a greater depth continued drilling caused gas flow (McConnell et al., 2010). This points out the sensitivity of Vulcan as a shallow surface resistivity mapper. The hydrate along the N-S tow is not expected until deeper in the section and is not detected by Vulcan here. However, there is evidence from well 'H' of shallow hydrate as well as nearby surface expressions of hydrate due to the proximity of a mud volcano, which may be the cause of the shallow resistors are detected along the E-W tow.

Figure 19 (top panel) shows a plot of the 0.5 Hz electric field data (red dots) and the 1D half-space forward models (red lines) for the E-W and N-S tows. The forward models are tracking the data well and are generally about 1 ohm-m except in a few places on the EW tow. This suggests that what we are observing in the N-S tow is real and that some of the higher frequencies in the E-W tow are giving the resistivity structure observed there.

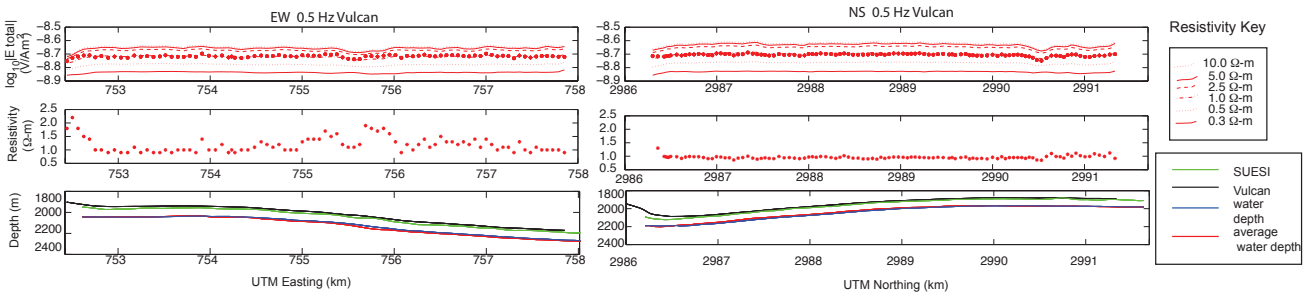

Figure 19: GC 955 EW and NS CSEM line for the 0.5 Hz Vulcan data and 1D half-space forward models (top), apparent resistivities (middle) and respective water depths to the transmitter (SUESI) and Vulcan as well as bathymetric profile.

2.3 Walker Ridge 313

WR313 is in intermediate water depths on the lower slope of the northern Gulf of Mexico, within a tabular salt minibasin province which has a very low geothermal gradient (hence a very thick gas hydrate stability

zone). Evidence for hydrate comes from seismic data, gas mounds, and focused fluid expulsion sites. The western region of the WR 313 basin is blocked by allochthonous salt to the south, east, and west, creating a closed basin allowing for the deposition of sand. Sediment enters from the north and builds up against the salt wall, creating dipping strata of fine grained clays, interbedded silts and fine grained sands in sheets and channel levee deposits (McConnell et al., 2010). Seismic data exhibits phase reversals in steeply dipping strata, which are interpreted as a transition from gas-charged sand to overlying gas-hydrate saturated sand (Hutchinson et al., 2008). Twenty OBEM receivers were deployed in two intersecting lines coincident with a 3D seismic volume, an industry well WR 313-001 and two subsequent JIP well locations 'G' and 'H' drilled in the spring of 2009 at site 4 ('G') and between sites 16 and 15 ('H').

Figure 20 contains a map view of the Walker Ridge 313 survey area with geologic annotations after Hutchinson et al. (2008) and pseudosections for frequencies of 0.5 Hz. Of note is the salt wall to the south and east where sites 9 and 14 are located.

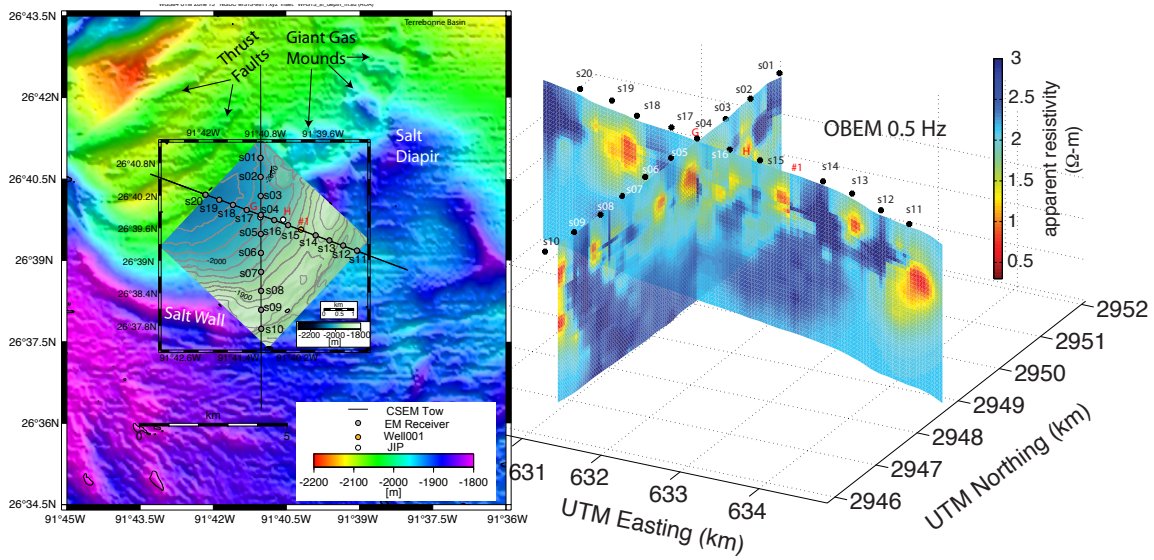

Figure 20: Walker Ridge 313 survey map with annotation from Hutchinson et al. (2008) (left) and OBEM pseudosection crossplots for 6.5 (top right) and 0.5 Hz (bottom right).

Pseudosections for Vulcan and 0.5 Hz and 6.5 Hz OBEM data are shown in Figure 21 for the EW (left) and NS (right) tows. The 6.5 Hz has a much shallower depth sensitivity and exhibits relatively little resistivity structure. Of note is the salt wall to the south and east where sites 9 and 14 are located. This salt wall is evident in the 0.5 Hz pseudosection as a resistor that extends downwards into the pseudosection; the fact that it is barely present in the 6.5 Hz is an indication that it has a deeper depth extent. Hydrates were found in both wells in the top of the seismic section as stratal-bound facture-filling gas hydrate and also within the dipping sheeted sands (horizons blue, orange, and green) deposits that occur deeper in the well (Boswell et al., 2009a). The pseudosections give resistive features under both 'G' and 'H' wells which could correspond with the JIP LWD resistivities. The pseudosections may be capturing the dipping strata, but further analysis is required before this can be quantified.

The Vulcan pseudosections and OBEM pseudosections at WR 313 give a consistent story with resistivies that are similar in value and similar in structure and crossing pseudosections tie together well. (Previous pseudosections (Phase 1) were made using inadequate transmitter navigation). The pseudosections shown here have been computing using the new transmitter geometry from the total field navigation program. With this update, there is a better agreement between the OBEM pseudosections and the new Vulcan pseudosections.

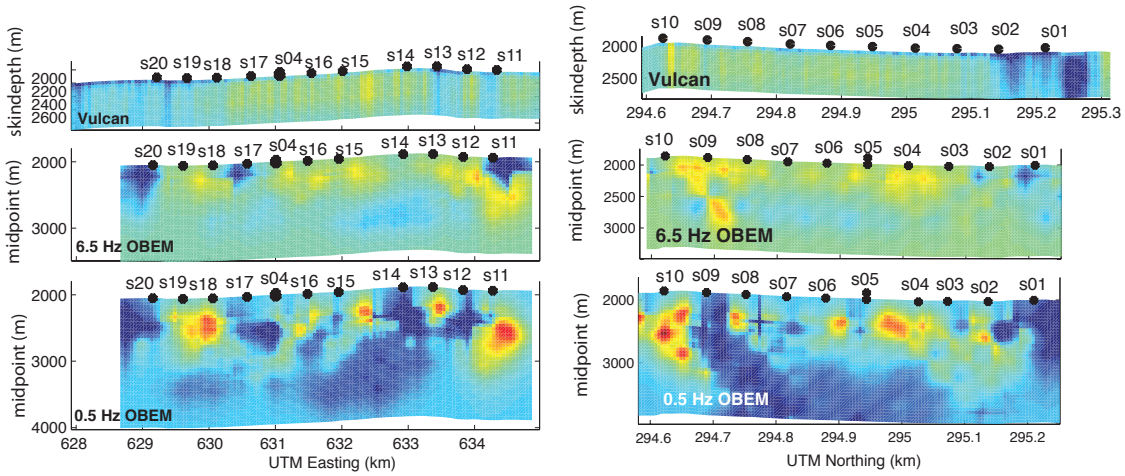

Figure 21: WR 313 EW CSEM line (left) and the WR 313 NS CSEM line (right) for the Vulcan data (top), 6.5 Hz OBEM data (middle) and 0.5 Hz OBEM data (bottom).

A closer look at the 0.5 Hz EW trending pseudosection is shown in Figure 22 with a corresponding EW seismic line from Boswell et al. (2009a). The JIP drilled two holes at WR313, 'G' and 'H', which are intersected by the EW CSEM line. Hydrates were found in both wells in the top of the seismic section as stratal-bound facture-filling gas hydrate and also within sheeted sands (Boswell et al., 2009a). The pseudosections give resistive features under both 'G' and 'H' wells, which could correspond with the JIP LWD resistivities. The pseudosections are perhaps capturing the dipping strata as shown in the seismic transect, but further analysis is required before this can be quantified.

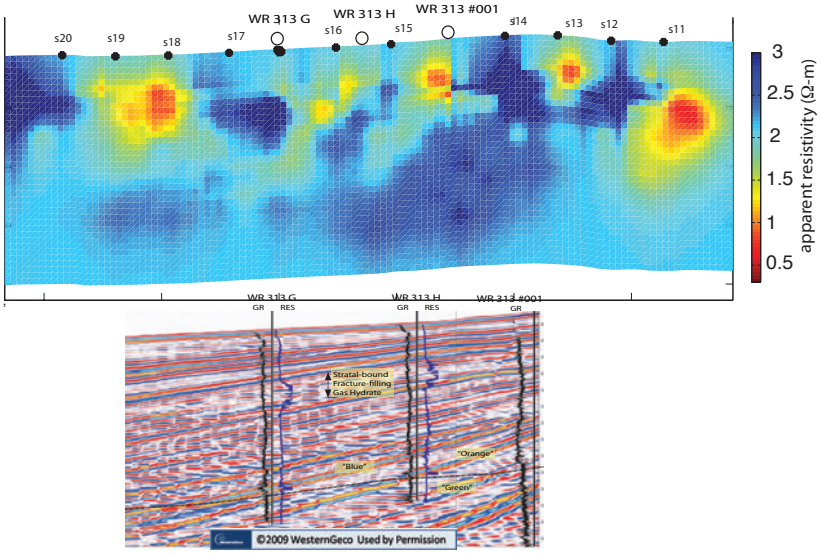

Figure 22: WR 313 EW-trending 0.5 Hz OBEM pseudosection and seismic line from Boswell et al. (2009a).

2.4 Mississippi Canyon 118

This block has been designated as a Minerals Management Services observatory. Large outcrops of hydrate occur on the seafloor in relatively shallow water depths of 800-900 m, but there is yet no direct evidence of hydrate at depth. This area provides the opportunity to coordinate and collaborate with many other ongoing

scientific programs, including shallow resistivity surveying. We deployed 24 receivers in a 6 x 4 array and towed 10 transmitter lines in a grid pattern (avoiding the already installed seafloor equipment) (Figure 23).

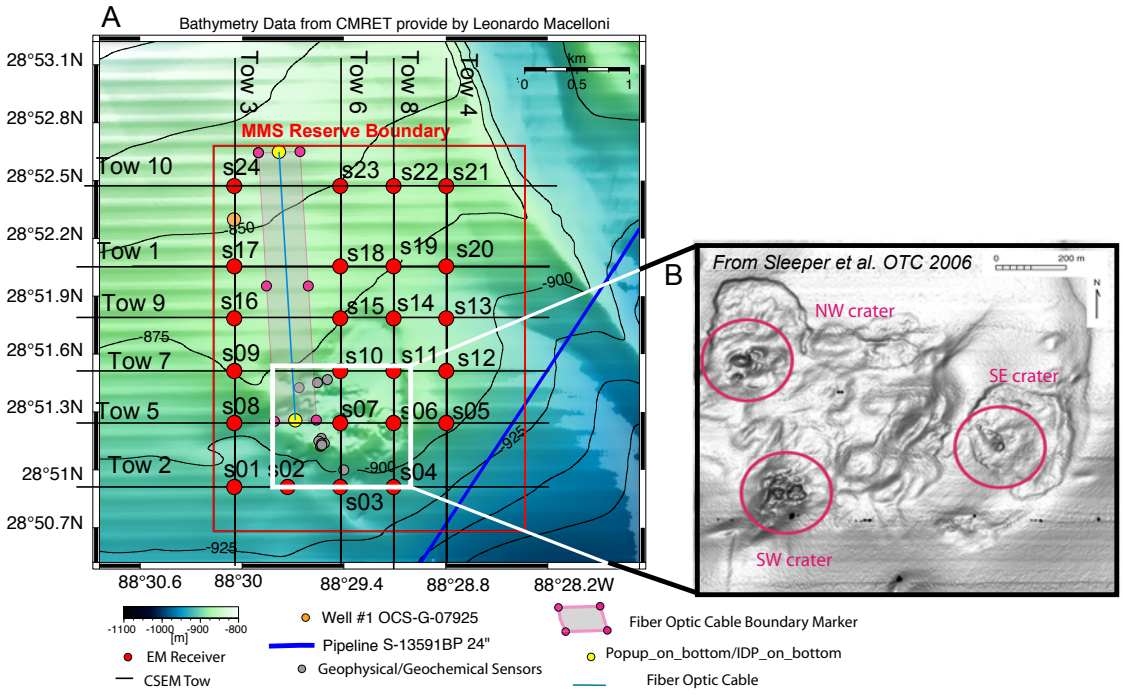

Figure 23: Survey map of Mississippi Canyon 118 with detail of the three crater complexes (bathymetry was provided by Leonardo Macelloni and the close up of the three crater complexes is from Sleeper et al., 2006).

MC 118 has been the main focus for Phase 2 due to its relatively flat seafloor bathymetry and generally bland resistivity structure except at the three main seafloor crater locations, allowing for simple 1D modeling and inversion of the CSEM data. Vulcan pseudosections for MC 118 are shown in Figure 24, and OBEM pseudosections are shown in Figure 25 for the old Marquardt (left) and the new OCCAM (right) navigation solution for the transmitter geometry.

MC 118 is conductive with a background resistivity of 0.5-1 Ωm and is generally featureless except at the SE crater. No constraints were placed on the intercepting tow lines and so the fact that three lines independently give a resistive body at the SE crater assures us that this is an attribute of the data due to geology. The EW line that crosses through the SE crater is overlayed on chirp acoustic line 119 from Sleeper et al. (2006) in order to compare acoustic blanking to electrical conductivity. The acoustic blanking or wipeout zones at MC 118 are attributed to authogenic carbonate as well as free gas and gas hydrate (Lapham et al. 2008). Carbonate rocks are present on the crater floors and have been noted in the SW crater (McGee et al. 2009 and 2008). The SE crater has a pavement of dead methanotrophic clams and there is no evidence for recent venting, which suggests that the conduit which once supplied methane to these clams became blocked, perhaps due to hydrate formation (McGee et al. 2009 and 2008). We find that the SE crater resistor appears to have some depth extent and the acoustic blanking there is associated with resistive structures. However, the acoustic blanking towards the SW crater (attributed to the shallow carbonates present there (Macelloni, pers comm.)) is associated with the background resistivity of 1 Ωm. This is significant, in that hydrate and carbonates, thought to be a confounding electrical resistors, are in fact differentiable here. Only drilling at the SE crater will confirm the presence of hydrate at depth.

The OBEM pseudosections for 6.5 Hz are shown in Figure 25 and give results consistent with the Vulcan

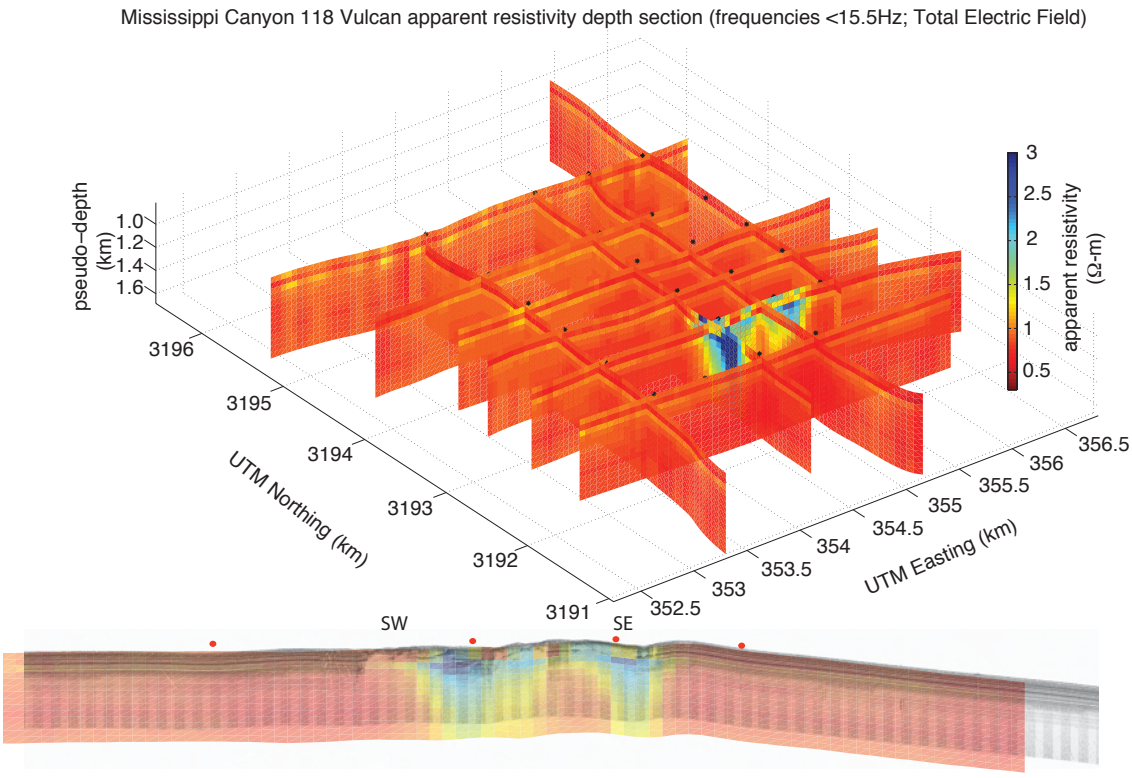

Figure 24: Apparent resistivity depth section based on frequency for Vulcan data collected at MC 118 and an EW transect from Line 5 overlayed on chirp acoustic data from Sleeper et al. (2006) which crosses the SE crater.

pseudosections. Three CSEM tow lines independently give a resistor at the SE crater with a background resistivity of about 1 Ω-m. The seafloor receiver data images the top few kilometers of sediment and the Vulcan data images the top 100's of meters. Seafloor background resistivies are slightly elevated in the OBEM data because they are sampling a larger sediment volume. The new navigation models show that inconsistencies in the OBEM pseudosections at the crossing points of NS and EW CSEM tow lines at site 9, were navigational errors.

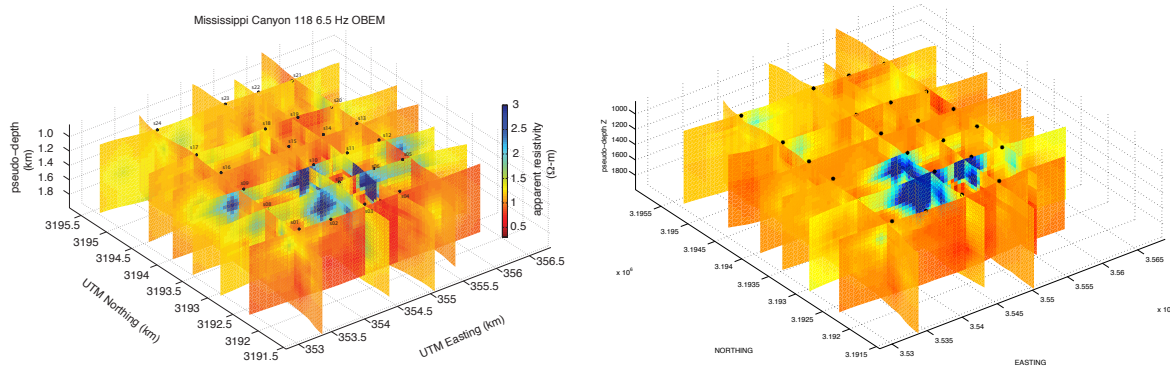

Figure 25: Mississippi Canyon 118 OBEM apparent resistivity pseudosections using Marquart TFN program (left), and OCCAM TFN (right). Notice the improved agreement of the crossing tow lines with the new OCCAM derived transmitter model.

3. 1D OCCAM inversions for MC 118

The relatively flat bathymetry at MC 118 means we can make 1D approximations for interpretation (compared to WR 313, GC 955 and AC 818 which have large bathymetric changes and far more complex resistivity structure). Over 100 1D OCCAM inversions have been computed for the MC 118 CSEM data, using a 30 node computer cluster. 1D OCCAM inversions were computed at each site using the rotated inline electric field component of multiple frequencies (0.5, 1.5, 2.5, 3.5, 6.5 and 13.5 Hz). The inversions at each site were further separated into an in-tow and out-tow inversion. The noise floor of the in-line electric field data was set to be 10% of the datum amplitude, and a tolerance of RMS =1.0 was requested of the inversion program. In most cases an RMS of 1.0 was achieved. However, in some instances the models appeared to be over fit and so the tolerance was relaxed. In other instances the inversion was unable to achieve the requested tolerance, and so the tolerance was relaxed until the inversion was able to converge to a smooth solution. Lines 5,6,8, and 9 in particular were unable to achieve a smooth 1D model with a tolerance of 1.0 . This is were most of the apparent resistivity structure occurs in the pseudosections, and is probably not well represented by a simple 1D model at each site. Nevertheless, site by site inversions help us to understand the data-set and guide our next steps in interpretation. The 1D OCCAM inversions are shown in the following Figures of the NS (Figures 26A, B) and the EW tows (Figures 27A, B, C), and are color coded purple for the transmitter in-tow to an OBEM and black for the transmitter out-tow. Be aware that the resistivity scale changes between the different lines.

Generally, all inversions put structure in the top 500 m of the 1D models, although all resistivities are below about 5 Ωm. In some instances, such as line 2 s05, and s01, there is not very much data for the in-tow and so the resistivity model is rather bland. Another feature common to most of the inversions is that they are generally very conductive, and almost all oscillate to have resistivities below seawater; which is probably an artifact of the fitting method. At about 1.5 km depth some models exhibit an increase in resistivity, which may be associated with the salt body known to be located beneath MC 118. The shallow surface changes in resistivity could be associated with hydrate.

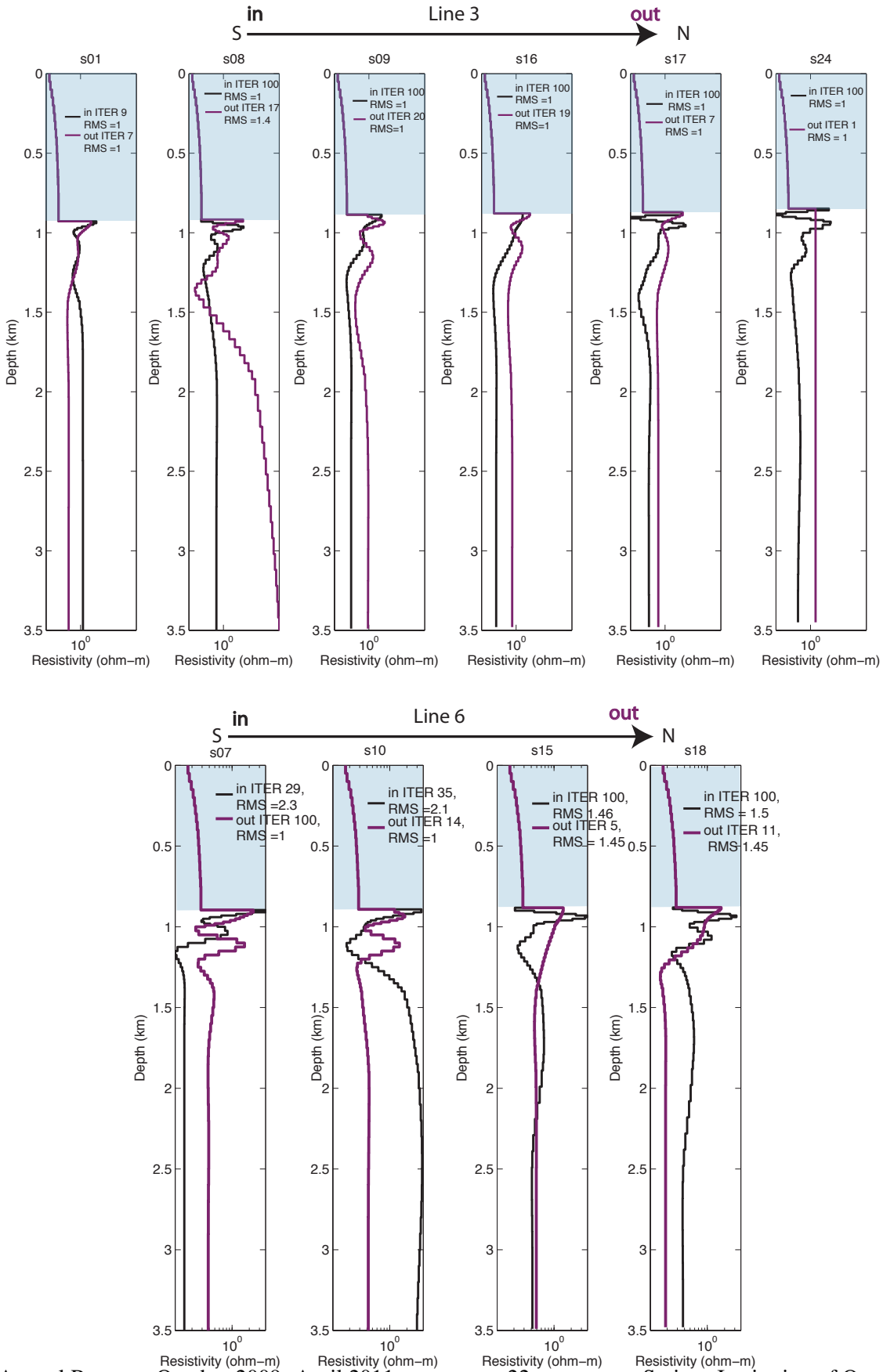

Figure 26A: NS OCCAM 1D inversions for Lines 3 and 6

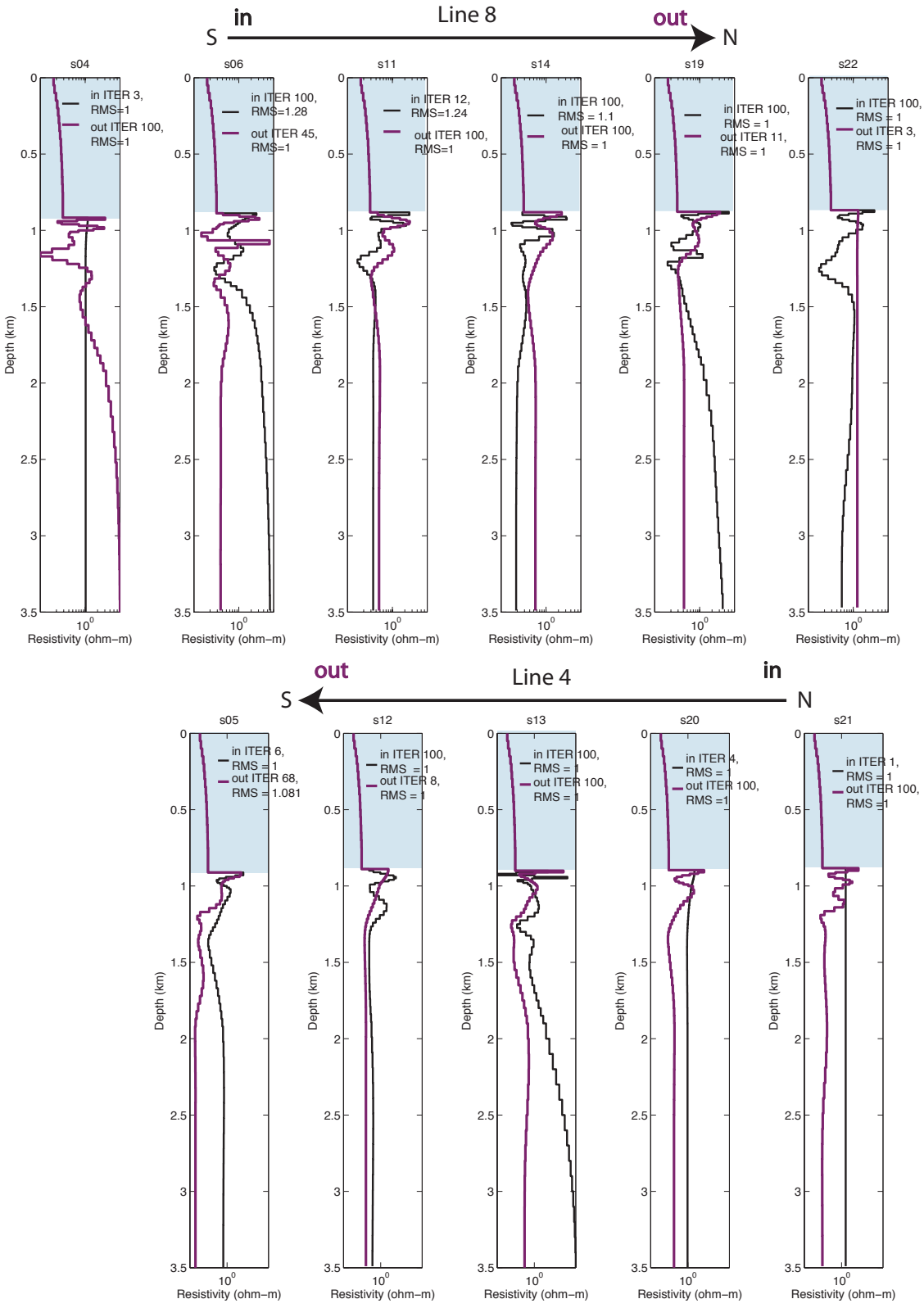

Figure 26B: NS OCCAM 1D inversions for Lines 8 and 4

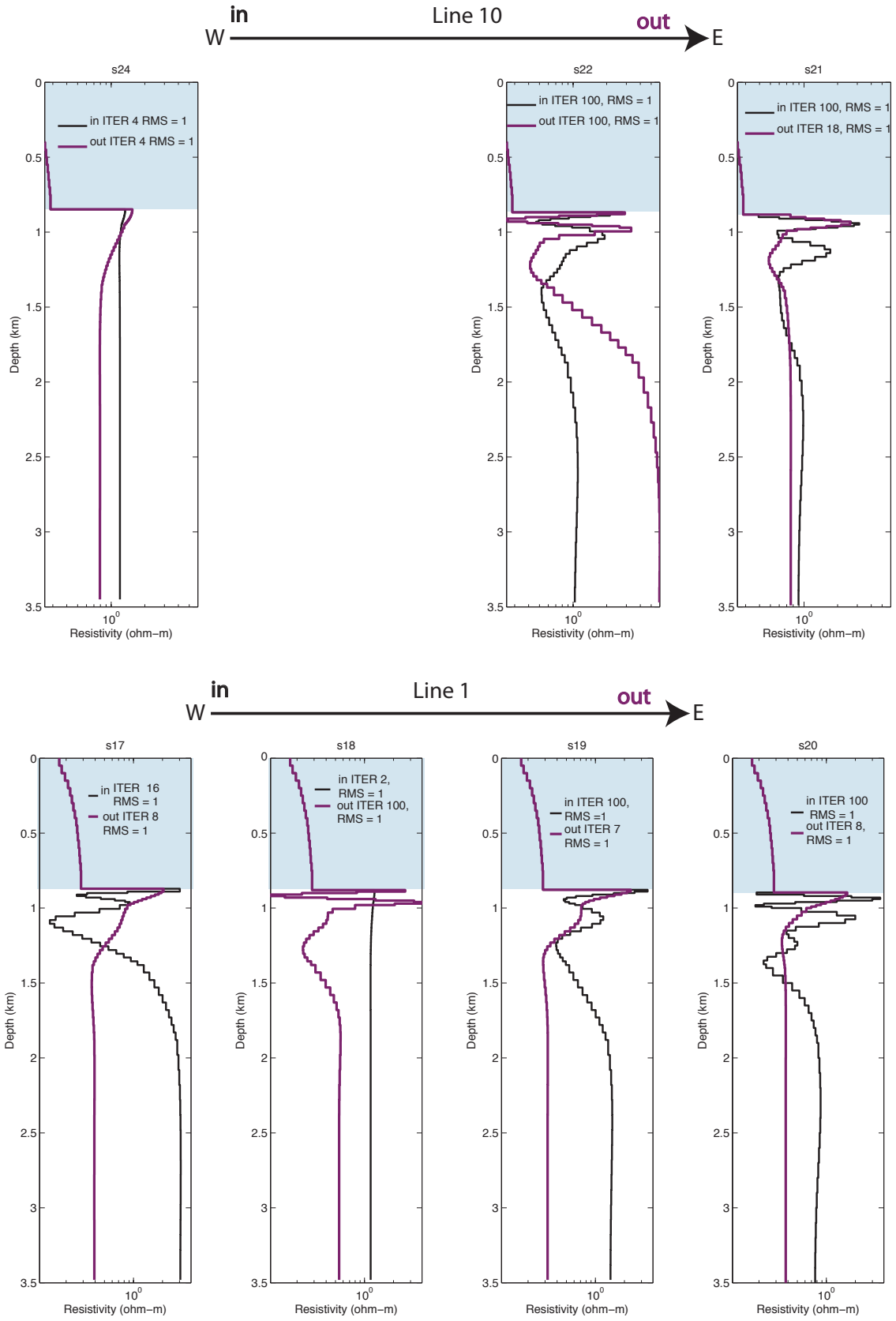

Figure 27A: OCCAM 1D inversions for EW Lines 10 and 1

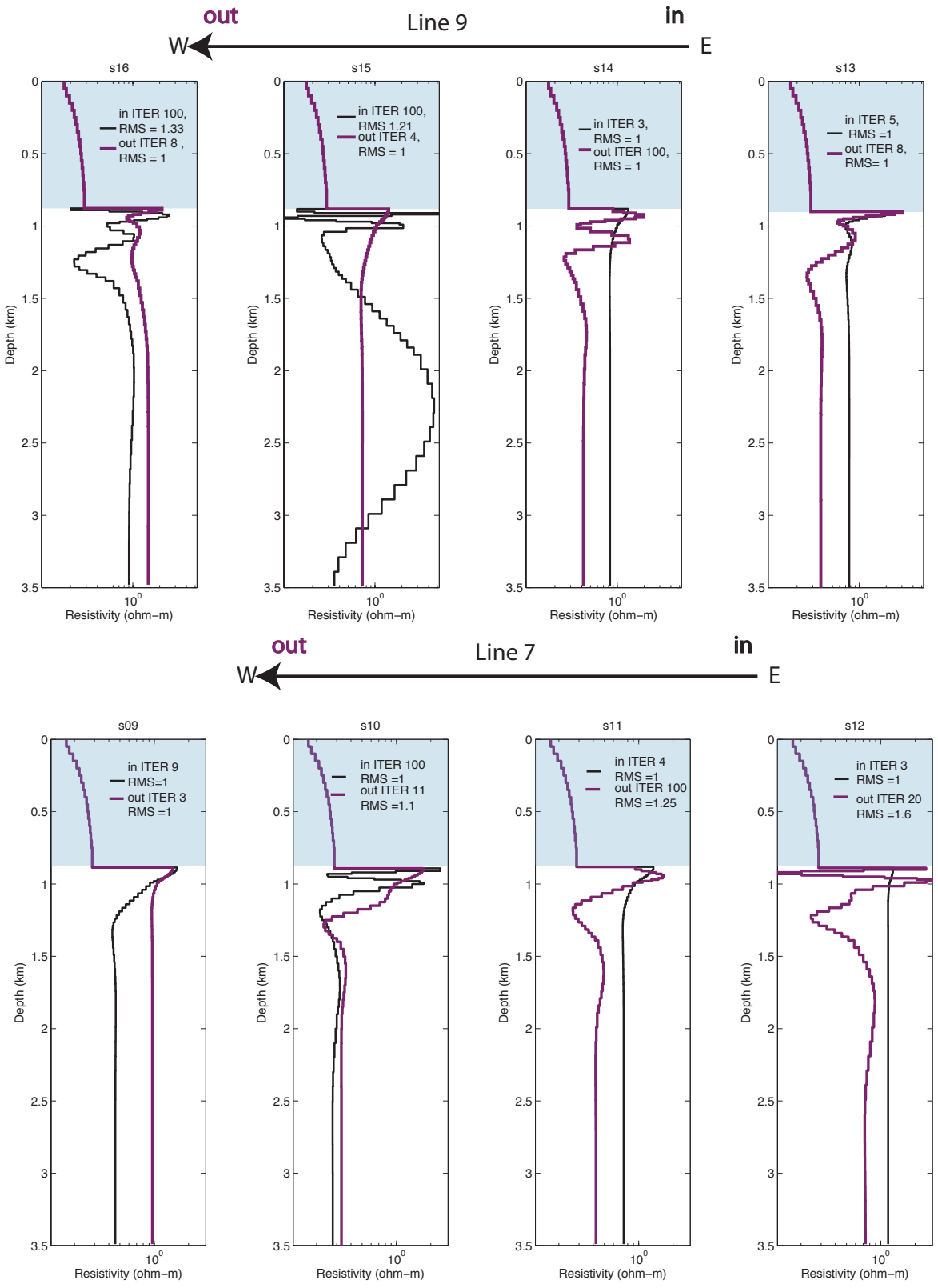

Figure 27B: OCCAM 1D inversions for EW Lines 7 and 9

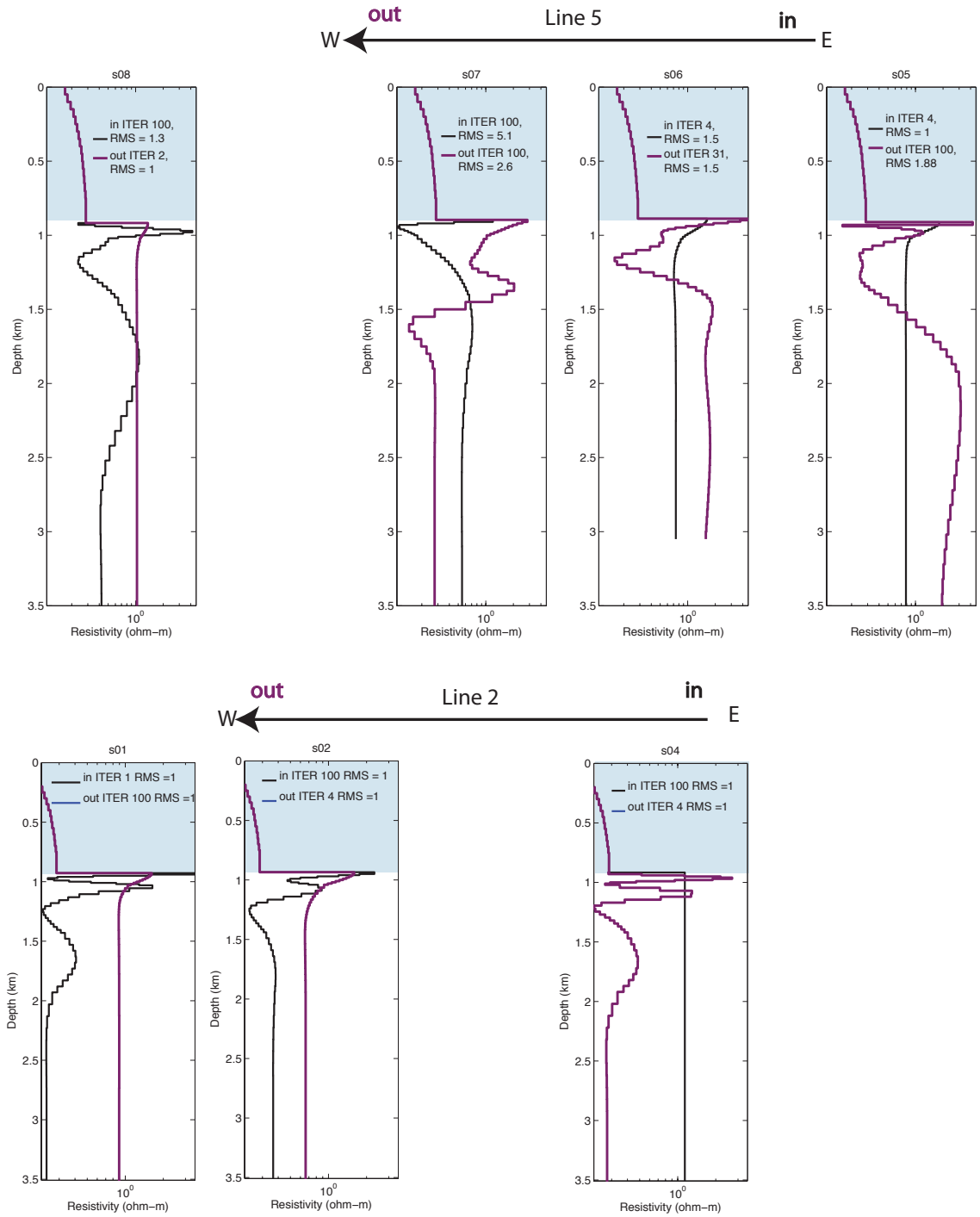

Figure 27C: OCCAM 1D inversions for EW Lines 5 and 2

4 2D Forward Modeling of Line 5 at MC 118

Along line 5, there are difficulties in reducing the RMS of the inversion to 1.0, suggesting that the 1D assumptions are no longer valid. For this reason we have started to implement 2D forward modeling of the CSEM data by using the 2D finite element modeling code of Li and Key (2007). To date only a 1 ohm-m

bathymetric half-space has been modeled along line 5 at a frequency of 0.5 Hz. The final finite element mesh is shown in the bottom panel of Figure 28 (note the 10 x vertical exaggeration). The electric fields of the 2D model have been rotated into the data coordinates, and plotted along with the CSEM data collected at each OBEM. In addition we include the 1D half-space forward model of the electric field amplitude. The black lines are the 2D model for 1 ohm-m (solid) and 0.3 ohm-m (dashed), and the colored lines are the 1D models for 1 ohm-m and 0.3 ohm-m. Note that the 0.3 ohm-m are slightly different, because a seawater electrical conductivity profile was not used in the 2D model, but was used for the 1D model. The 1 ohm-m of the 1D and 2D models are due to both bathymetric effects and the different seawater conductivity profiles used. Site 7 is most affected by the bathymetry, at ranges greater than 1km. The electric field amplitude of the major axis of the polarization ellipse (Pmax) is less sensitive to the bathymetric effects than the individual components, and so our initial pseudosections are still valid.

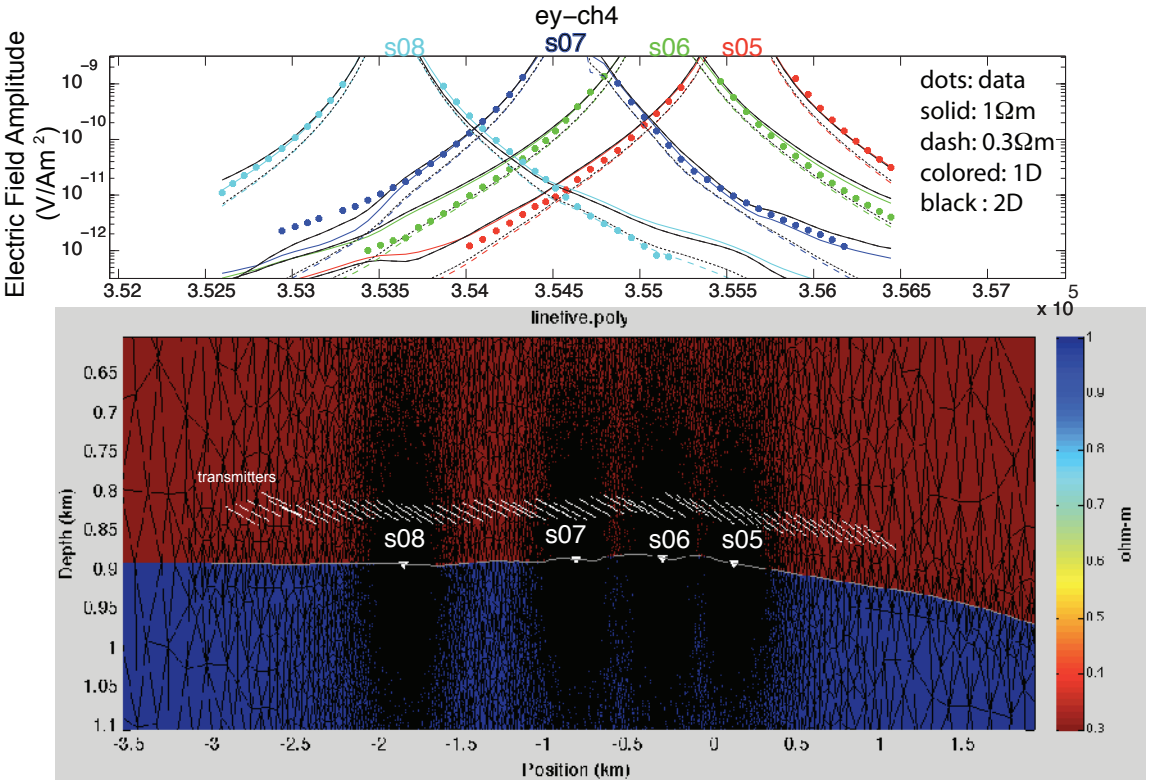

Figure 28: A 1 Ωm 2D bathymetric forward models for line 5 at MC 118. Top is the electric field amplitudes for 2D, 1D models and the recorded data at each of the sites. The bottom panel is the final mesh with about a 10 x vertical exaggeration.

References: Boswell, R., Collett, T., Frye, M., McConnell, D., Shedd, W., Mrozewski, S., Guerin, G. and Cook, A. [2010] Gulf of Mexico Gas Hydrate Joint Industry Project Leg II: Technical Summary.

http://www.netl.doe.gov/technologies/oil-gas/FutureSupply/MethaneHydrates/JIPLegII-IR/

Cook, A., G. Guerin, S. Mrozewski, T. Collett, R. Boswell. 2010. Gulf of Mexico Gas Hydrate Joint Industry Project Leg II: Walker Ridge 313 LWD Operations and Results.

Key, K. [2009] 1D inversion of multicomponent, multifrequency marine CSEM data: Methodology and synthetic studies for resolving thin resistive layers. Geophysics, 74(2) F9-F20.

McConnell, D., Boswell, R., Collett, T., Frye, M., Shedd, W., Guerin, G., Cook, A., Mrozewski, S., Dufrene, R. and Godfriaux, P. [2010] Gulf of Mexico Gas Hydrate Industry Project Leg II: Green Canyon 955 Site Summary. http://www.netl.doe.gov/technologies/oil-gas/FutureSupply/MethaneHydrates/JIPLegII-IR/

McConnell, D., R. Boswell, T. Collett, M. Frye, W. Shedd, G. Guerin, A. Cook, S. Mrozewski, R. Dufrene, P. Godfriaux. 2010. Gulf of Mexico Gas Hydrate Joint Industry Project Leg II: Walker Ridge Site Summary.

Bowsell, R., T. Collett, D. McConnel, M. Frye, B. Shedd, S. Mrozewski, G. Guerin, A. Cook, P. Godfriaux, R. Dufrene, R. Roy and E, Jones. 2009a. Joint Industry Project Leg II Discovers Rich Gas Hydrate Accumulations in San Reservoirs in the Gulf of Mexico. in *Fire in the Ice* pages 1-5.

Bowell, R., D. Shelander, M. Lee, T. Latham, T. Collett, G. Guerin, G. Moridis, M. Reagan and D. Golderberg. 2009b. Occurrence of gas hydrate in Oligocene Frio sand: Alaminos Canyon Block 818: Northern Gulf of Mexico. *Marine and Petroleum Geology,* doi:10.1016/j.marpetgeo.2009.03.005.

Fiduk, J.C., P. Weimer, B.D. Trudgill, M. G. Rowan, P. E. Gale, R. L. Phair, B. E. Korn, G. R. Roberts, W. T. Gafford, R. S. Lowe, and T. A. Queffelec. 1999. The perdido fold belt , northwestern deep Gulf of Mexico, Part 2: seismic stratigraphy and petroleum systems. *American Associated of Petroleum Geologists Bulletin.* V. 83. No. 4 (April 1999) P. 578-612.

Hutchinson D.R., D. Shelander, J. Dai, D. McConnell, W. Shedd, M. Frye, C. Ruppel, R. Boswell, E. Jones, T. Collett, K. Rose, B. Dugan, W. Wood, T. Latham. 2008. Site Selection for DOE/JIP Gas Hydrate drilling in the northern Gulf of Mexico. *Proceedings of the 6th International Conference on Gas Hydrates (ICGH 2008),* Vancouver, British Columbia, Canada July 6-10 2008.

Jones, E., T. Latham, D. McConnell, M. Frye, J. Hunt Jr., W. Shedd, D. Shelander, R. Boswell, K. Rose, C. Ruppel, D. Hutchinson, T. Collett, B. Dugan, W. Wood. 2008. Scientific Objectives of the Gulf of Mexico Gas Hydrate JIP Leg II Drilling.*Offshore Technology Conference* Paper No. 19501.

Key, K. 2009. 1D inversion of multicomponent, multifrequency marine CSEM data: Methodology and synthetic studies for resolving thin resistive layers. *Geophysics* Vol. 74. No. 2 (March-April 2009)

Laphan, L.L., J.P. CHanton, C.S. Martens, K. Sleeper and J.R. Woolsey. 2008. Mircobial activity in surficial sediments overlying acoustic wipeout zones at a Gulf of Mexico cold seep. *Geochemistry, Geophysics, and Geosystems* Vol. 9. No. 6 (4 June 2008) Q06001, doi:10.1029/2008GC001944 ISSN 1525-2027

Latham, T. and D. Shelander, R. Boswell, T. Collett, M. Lee. 2008. Subsurface Characterization of the hydrate bearing sediemnts near Alaminos Canyon 818. *Proceedings of the 6th International Conference on Gas Hydrates (ICGH 2008),* Vancouver, British Columbia, Canada July 6-10 2008.

McGee, T., J.R. Woolsey, L. Lapham, R. Kleinberg, L. Macelloni, B. Battista, C. Knapp, S. Caruso, V. Goebel, R. Chapman, P. Gerstoft. 2008. Structure of a carbonate/hydrate mound in the northern Gulf of Mexico. *Proceedings of the 6th International Conference on Gas Hydrates (ICGH 2008),*Vancouver, British Columbia, Canada July 6-10 2008.

McGee, T., J.R. Woolsey, C. Lutken, L. Macelloni, L. Lapham, B. Battista, S. Caruso, V. Geobel. 2009. A multidisciplinary seafloor observatory in the northern Gulf of Mexico: results of preliminary studies. http://www.olemiss.edu/depts/mmri/programs/multidisciplinary.pdf

Sleeper, K. A. Lowrie, A. Bosman, L. Macelloni, C.T. Swann. 2006. Bathymetric mapping and high resolution seismic profiling by AUV in MC 118 (Gulf of Mexico). *Offshore Technology Conference.* OTC-18133. May 1-4, 2006. data made available at:

$http://www.olemiss.edu/depts/mmri/programs/mc118/pro\_map.html$

Smith, S., R. Boswell, T. Collett, M. Lee, and E. Jones. 2006. Alaminos Canyon Block 818: A documented example of gas hydrate saturated sand in the Gulf of Mexico. *Fire In the Ice* Fall 2006. Pages 12-13.

Task 8.0: Estimate Quantitative Hydrate Volumes from Field Models and Laboratory Studies.

Hydrate volume estimates have been made for MC 118 using Archie's Law and the Hashin-Shtrikman mixing laws. The geologic and bathymetric structures in the other prospects are too complicated to make reliable hydrate volume estimates at this time.

Archie's Law is defined as:

$$\rho_t = a\phi^{-m}\rho_w / {S_w}^n \tag{1}$$

where a is the tortuosity factor, m is the cementation exponent of the rock, n is the saturation exponent, ϕ is the porosity, ρ_w is the resistivity of the pore fluid, S_w is the fluid saturation, and ρ_t is the measured resistivity (Archie 1942). We set m = 2, n = 2, and a = 1 for our computations.

We can use Archie's Law to estimate the porosity of the sediment as a function of depth, by assuming the sediment is fully saturated with water (S_w= 1) (Ellis et al, 2008). This simplifies equation (1) to:

$$\rho_t = \phi^{-m}\rho_w(T, S) \tag{2}$$

where the pore fluid resistivity, $\rho_w(T, S)$, now varies as a function of temperature, T and salinity, S, based on the equation of state for seawater. The temperature as it varies with depth can be predicted from seafloor temperature ($4°C$ (Lapham, 2010)) and the geothermal gradient measured in the ARCO well at MC 118 of 17.2° C/km (Knapp et al. 2010, AAPG presentation). An estimate of the pore fluid conductivity at the seafloor is given from the transmitter CTD. Arps Law is then used to predict the fluid resistivity as a function of temperature (depth) (Collett and Ladd, 2000; Arp, 1953):

$$\rho_w(z) = \rho_w(0)(T(0) + 21.5°C)/(T(z) + 21.5°C) \tag{3}$$

where z = 0 is the surface of the seafloor. Finally, at MC 118 the background resistivity is about 1Ω-m and so we use this resistivity value for ρ_t. This further simplifies equation (2) and allows us to solve for porosity as a function of depth.

$$\phi = \rho_w(T, S)^{1/m} \tag{4}$$

Figure 29 shows the temperature, fluid resistivity and Archie predicted porosity-depth profiles.

Using the Archie calculated porosity for the region we can then rearrange equation 1 to solve for water saturation S_w:

$$S_w(z) = ((a\rho_w(z)\phi(z)^{-m}/\rho_t(z)))^{1/n} \tag{5}$$

but this time ρ_t represents our CSEM apparent resistivities as shown in Figure 25 (right). Finally a hydrate saturation, S_h, can be computed:

$$S_h(z) = 1 - S_w(z). \tag{6}$$

This techinque is similar to that used by the Ocean drilling program (Shipboard Scientific Party, 2003; Collett, 1998). Figure 31 (left) shows the hydrate volume estimates based on Archie's Law.

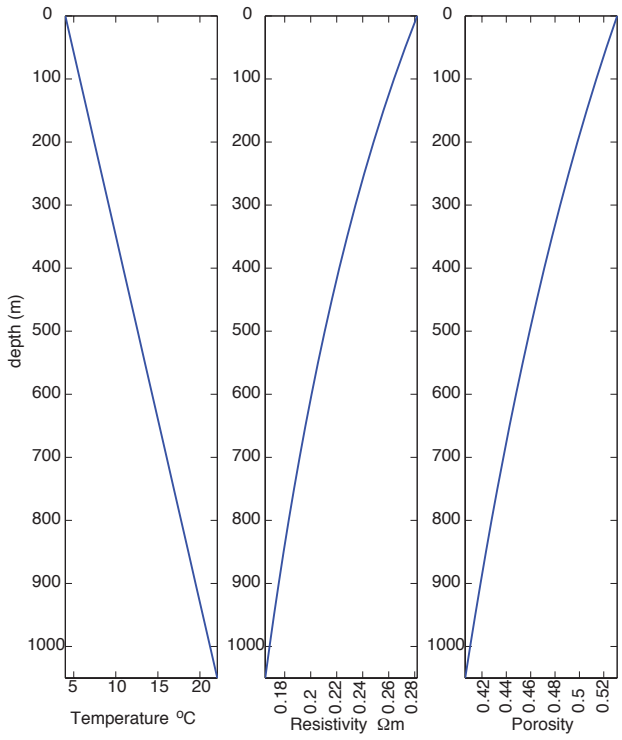

Figure 29 The temperature-depth profile, fluid resistance, and Archie predicted porosity-depth profile assuming a rock resistivity of 1Ω-m

Another way to compute hydrate saturation is through the Hashin-Shtrikman binary mixing laws, which are the extremal bounds (HS-bounds) for effective conductivity, σ (Schmeling 1986; Hashin & Shtrikman 1963):

$$\sigma_{HS}{}^{-} = \sigma_s + (\beta)(1/(\sigma_f - \sigma_s) + (1-\beta)/(3\sigma_s))^{-1}; \quad (7)$$

$$\sigma_{HS}{}^{+} = \sigma_f + (1-\beta)(1/(\sigma_s - \sigma_f) + \beta/(3\sigma_f))^{-1}; \quad (8)$$

where β is the volumetric fraction of the fluid and σ_s and σ_f are the specific conductivities of the matrix solid and the fluid. The HS upper bound, $\sigma_{HS}{}^{+}$ corresponds to a connected fluid phase (conductive) with isolated solid phase (resistive) and the HS lower bound, $\sigma_{HS}{}^{-}$, corresponds to isolated spherical fluid inclusions (conductive) within a solid matrix (resistive) (Hashin & Shtrikman 1963). In terms of hydrate, the HS upper bound may represent a low concentration of granular disseminated hydrate distributed in isolated spheres within the conductive sediment. In clay-rich sediments hydrate may occur in veins or fractures and be better represented by the HS lower bound — where resistive material occurs in sheets impeding current flow through the matrix of fluid. Here we assume the water saturated sediments are the fluid phase, σ_f and that the hydrate is the solid phase, σ_s. We use the Arrhenius relationship and the constants from the laboratory conductivity measurements of run 3 in Table 1 in order to compute a hydrate resistivity as a function of the geothermal gradient (Figure 30 right). The lower bound predicts resistivities that are higher than what we measure and so does not predict a useful hydrate volume. The upper bound which represents resistive inclusions within a conducting matrix does yield a sensible hydrate volume. The $\sigma_{HS}{}^{+}$, can be rewritten in terms of resistivity:

$$\rho_{HS}{}^{+} = 1/\sigma_{HS}{}^{+}. \quad (9)$$

We compute $\sigma_{HS}{}^{+}$ values for a range of β values between 0 and 1 and then find the $\rho^{+}_{HS}(\beta)$ that best fits the

CSEM apparent resistivities. We essentially create a look up table for resistivity and β, as shown in Figure 30. Figure 31 (right), shows the hydrate volume estimates predicted by the HS+ bound.

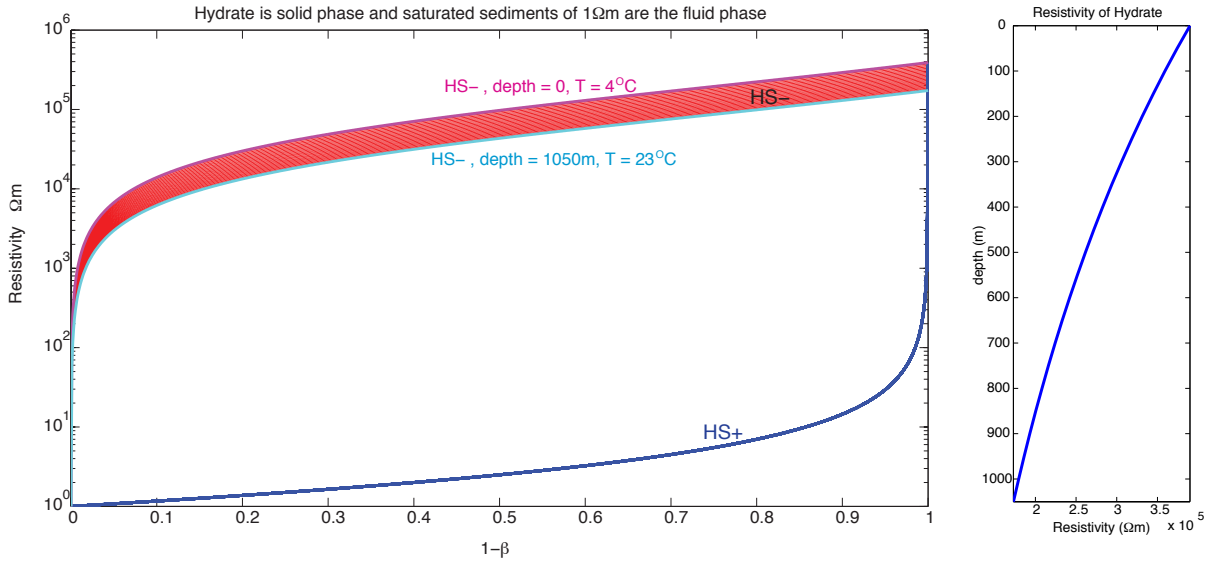

Figure 30: The HS bounds for hydrate and 1Ωm fluid saturated sediment, versus hydrate volume fraction (left) and the laboratory measured hydrate resistivity based on temperature which has been converted into depth by the geothermal gradient measured in the ARCO well (right).

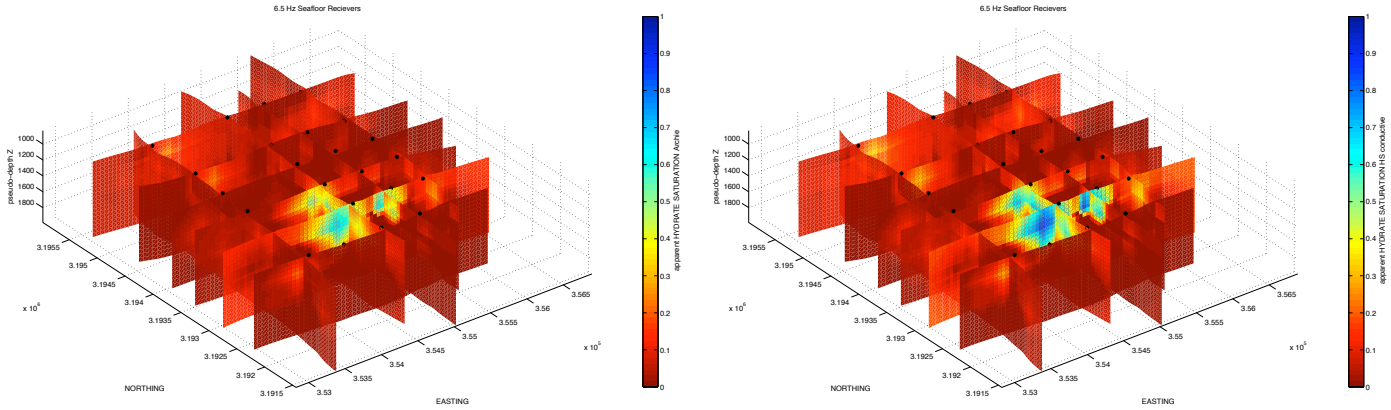

Figure 31: Apparent hydrate concentrations based on Archies Law (left) and the HS upper bound (right).

Archies Law lies between the HS upper and lower bounds and so the HS upper bound predictions of hydrate volume are slightly greater then those predicted by Archies Law. There is a general concentration of hydrate between 40 and 80% at the crater locations for MC 118. The remaining area is generally bland with very little hydrate predicted.

References

Archie, G. E., 1942. The electrical resistivity log as an aid in determining some reservoir characteristics, Transactions of the American Institute of Mining and Metallurgical Engineers, 146, 54—62.

Arps, J., 1953. The effect of temperature on the density and electrical resistivity of sodium chloride solutions, Petroleum Transactions, AIME, 198, 327—330.

Collett, T., 1998. Well log evaluation of gas hydrate saturations, in SPWLA 39th Annual Logging Symposium, pp. 1—14.

Collett, T. S. & Ladd, J., 2000. Detection of gas hydrate with downhole logs and assessment of gas hydrate concentrations (saturations) and gas volumes on the Blake Ridge with electrical resistivity log data, Proceedings of the Ocean Drilling Program, Scientific Results, 164, 179—191.

Ellis, M., Evans, R., Hutchinson, D., Hart, P., Gardner, J., & Hagen, R., 2008. Electromagnetic surveying of seafloor mounds in the northern gulf of mexico, Marine and Petroleum Geology, 25, 960—968.

Hashin, Z. & Shtrikman, S., 1963. A variational approach to the theory of the elastic behaviour of multiphase materials, Journal of Mechanics of Physical Solids, 11, 127—140.

Knapp James H., Camelia C. Knapp, Leonardo Macelloni, Antonello Simonetti, and Carol Lutken Subsurface Structure and Stratigraphy of a Transient, Fault-Controlled Thermogenic Hydrate System at MC-118, Gulf of Mexico Search and Discovery Article #50356 (2010) Posted November 22, 2010 Adapted from an oral presentation at AAPG Annual Convention and Exhibition, New Orleans, Louisiana, USA, April 11-14, 2010

Lapham, LL., JP Chanton, R. Chapman, CS Martens, 2010. Methane under-saturated fluids in deep-sea sediments: Implications for gas hydrate stability and rates of dissolution. Earth and Planetary Science Letters 298 (2010) 275—285.

Shipboard Scientific Party, 2003. Proceedings ODP, Initial Reports, in Leg 204 Summary, vol. 204, chap. Leg 204 summary, pp. 1—75, eds Trehu, A. M., Bohrmann, G., Rack, F. R., Torres, M. E., & et al., Ocean Drilling Program, College Station TX.

Schmeling, H., 1986. Numerical models on the influence of partial melt on eleastic and anelastic and electrical properties of rocks. Part II: electrical conductivity, Physics of the Earth and Planetary Interiors, 43, 123—136.

Task 9.0: Technology Transfer. The data have been distributed to the sponsors (February, 2009) and preliminary results were presented at the Seafloor Electromagnetics Consortium annual meeting March 18 and 19, 2009, and 2010, 2011. Constable attended the 2009 SEG meeting and generated interest in further research in developing Vulcan systems. A poster was presented at the 2009 Fall AGU Meeting. Version 1.0 of the transmitter navigation was distributed to sponsors in early December. Processed data with merged navigation was distributed to sponsors in late March 2010. Results were presented at the 2010 EM workshop in Egypt and published in First Break. Laboratory results have been accepted for publication in Geophysical Research Letters for the spring of 2011. Several abstracts have been submitted to the MARELEC meeting, June 2011 and the IGHC in July 2011.

Task 10.0: Final Publication. This task is scheduled for Budget Period 3.

CONCLUSION During phase 2 of this project we built the conductivity cell and made calibration runs on ice and teflon. We made three runs on gas hydrate and two runs on various hydrate-sediment mixtures. It would be useful to continue this work. The laboratory results were used to generate hydrate concentrations for MC 118. The navigational parameters for the transmitter have been recomputed using an OCCAM TFN program for the CSEM field data and improvements are most evident in the agreement at crossing towlines. 1D inversions of MC118 have been made and there is evidence of a surface resistor (hydrate), and a deeper resistor (salt), but generally all of these inversions require some high conductivities, which could

be an inversion artifact. We presented apparent resistivity pseudosections for all surveys, but 2D analysis is required for remaining surveys to gain more quantitative interpretations.

MILESTONE STATUS

Milestone log for Budget Period 2. October 1, 2009- March 31, 2011

Milestone 10: Design conductivity and pressure cell. Task 5.0, completed 15 January, 2010. Critical milestone for tasks 6, 8, 9, 10.

Milestone 11: Construct conductivity/pressure cell. Task 5.0, completed 30 April 2010. Critical milestone for tasks 6, 8, 9, 10.

Milestone 12: Make calibration tests of cell using water standard. Task 5.0, completed 30 July, 2010. Critical milestone for tasks 6, 8, 9, 10.

Milestone 13. Install cell in Menlo Park and make initial hydrate measurements. Task 5.0, completed October, 2010. Critical milestone for tasks 6, 8, 9, 10.

Milestone 14. Make at least two runs of measurements on conductivity cell Task 6.0, completed December, 2010. Critical milestone for tasks 8, 9, 10.

Milestone 15. Quantitative modeling of conductivity results. Task 6.0, completed February 2011. Critical milestone for tasks 8, 9, 10.

Milestone 16. SEG abstract submitted. Tasks 9, 10, to be completed by abstract deadline (April 2010). Replaced this for an abstract submitted to the IAGA Electromagnetic Induction Workshop in Cairo, Egypt, in September 2010

Milestone 17. Quantitative resistivity modeling of field data. Task 7.0, Completed April 2011. Critical milestone for tasks 8, 9, 10.

Milestone 18. Conductivity results report Task 6.0, completed 30 March 2011. This is embodied in a Geophysical Research Letters paper and ICGH conference paper.

Milestone 19. Geological modeling and hydrate volume estimation Task 8.0,completed April 2011. Critical milestone for tasks 9, 10.

Milestone 20. Web page updated Task 9.0, completed April 2011.

*Milestone 21. Produce Phase 2 report.*Tasks 6—8, completed April 2011.

Milestone 22. Fall AGU abstracts submitted. Tasks 9, 10, to be completed by abstract deadline (Sept 2010). Replaced this with two abstracts submitted to the International Conference on Gas Hydrates held in Edinburgh, July 2011. An abstract was also submitted to the MARELEC meeting which will be held in La Jolla, June 2011.

ACCOMPLISHMENTS

- Collection of the Marine CSEM Field Data

- Conductivity cell completed.

• Processing of the data is completed.

• Two Fire in the Ice article were published, one in 2009 and the other in 2010.

• Participated in a "Spot Light on Research" article for Fire in the Ice in 2009.

• Raw data and processed data have been distributed to sponsors (2009, 2010).

• Generated merged transmitter navigation with the CSEM data using preliminary navigation models and distributed this version to the sponsors in early December 2009 and March 2010.

• Generated pseudosections for the 0.5 Hz and 6.5 Hz CSEM data transmissions for all 14 tows of the 4 surveyed areas in the Gulf of Mexico 2010.

• Generated pseudosections for Vulcan at MC 118, GC 955, AC 818, and WR 313 and preliminary interpretations of the data, 2010.

• First Break article published this June (2010).

• Completed calibration tests of cell using water standard.

• Installed the cell in Menlo Park, formed hydrate in the cell, and produced SEM images of this sample.

• Made electrical conductivity measurements on three hydrate samples.

• Published a Geophysics paper: "The practical application of 2D inversion to marine controlled source electromagnetic data"

• A Geophysical Research Letters paper is in press: "Electrical Properties of Polycrystalline Methane Hydrate" by Wyatt Louis Du Frane, Laura A Stern, Karen A. Weitemeyer, Steven C Constable, John C. Pinkston, Jeffery J. Roberts

PROBLEMS OR DELAYS The design and construction of the conductivity cell was given a six month extension in 2009. We have now successfully made several electrical conductivity measurements on hydrate and hydrate-sediment mixtures. However, we have discovered that because of the large sample size, these runs are taking much longer to equilibrate the anticipated, reducing the total number of runs we can make in the proposed project period. Improvements to the transmitter navigation by using a 1D OCCAM total field navigation code is working and results are close to being complete for all surveys. Volume estimates and 1D inversions have been made for MC 118, where 1D assumptions are valid. However, WR 313, GC 955 and AC 818 will require 2D or even 3D modeling and inversion to derive hydrate volume predictions from the EM data.

PRODUCTS

• Revised Project Management Plan.

• A project website was set up:

http://marineemlab.ucsd.edu/Projects/GoMHydrate/index.html

Cruise Report is available for download.

• Project Summary:

project summary outlining project goals and objectives on the NETL project Web site.

• Collection of Marine CSEM data in the Gulf of Mexico:

Data distributed to sponsors early February.

• Fire in the Ice article published Winter 2009.

• NETL kick off meeting, Morgantown, WV - January 6, 2009

The PI delivered a project overview presentation.

• Talk given at the 2009 MARELEC Meeting - Stockholm, Sweden - July 7-9 2009

Steve Constable presented *Applying marine EM methods to gas hydrate mapping*

• Submitted the first quarter report February 2 2009.

•Steve Constable gave an invited talk at LLNL mid march 2009 called:

Marine Electromagnetic Methods for Mapping Gas Hydrate

• SIO Seafloor Electromagnetics Consortium annual meeting, La Jolla, CA - March 18-19, 2009

Karen Weitemeyer delivered two presentations:

Marine EM for gas hydrate studies, with first results from the Gulf of Mexico

Using Near field data to navigate controlled source electromagnetic data

• Submitted the second quarter report April 2009.

• Karen Weitemeyer gave two invited talks in Australia

Marine EM for gas hydrate studies, with first results from the Gulf of Mexico

• Submitted the third quarter report July 2009.

Steven Constable delivered a presentation in Japan:

Marine Electromagnetic Methods for Mapping Gas Hydrate

• Submitted the Phase 1 report October 2009.

• AGU Poster presentation December 2009 by Karen Weitemeyer and Steven Constable

Marine EM for gas hydrate studies, with first results from the Gulf of Mexico

• DoE Atlanta Hydrate Meeting January 25-29, 2010. A talk and Poster presented by KW and SC

Applying Marine EM Methods the Gas Hydrate Mapping

• Fire in the Ice article published March 2010.

Test of a new marine EM survey method at Mississippi Canyon 118, Gulf of Mexico

• SIO Seafloor Electromagnetics Consortium annual meeting, La Jolla, CA - March 17-18, 2010

Karen Weitemeyer and Steven Constable delivered a presentation:

Results from the GoM gas hydrate studies

• Processed data distributed to sponsors late March, 2010 and early April, 2010.

• First Break Article published this June (2010).

Mapping shallow geology and gas hydrate with marine CSEM surveys

• Attended the 20th Electromagnetic Induction Workshop in Giza, Egypt September 18-25, 2010, and presented a poster.

Mapping gas hydrates and shallow sedimentary structure in the Gulf of Mexico using marine CSEM

• Submitted two abstracts to the 7th International Conference on Gas Hydrates (ICGH7), July 2011.

One by Constable, Du Frane, Pinkston, Weitemeyer, Roberts, Stern, Durham, on

Electrical resistivity of laboratory-synthesized methane hydrate

The second by Weitemeyer and Constable on

The development of marine electromagnetic methods for gas hydrate mapping

• Geophysics paper published this Fall (2010).

• Abstract submitted to the 2011 MARELEC Meeting - San Diego, USA - June 20-23 2011

• Geophysical Research Letters paper accepted for publication this spring (2011). Electrical Properties of Pure, Polycrystalline Methane Hydrate Wyatt L. Du Frane, Laura A. Stern, Karen A. Weitemeyer, Steven C. Constable, John C. Pinkston, Jeffrey J. Roberts

Acknowledgment: "This material is based upon work supported by the Department of Energy under Award Number DE-NT0005668."

National Energy Technology Laboratory

626 Cochrans Mill Road
P.O. Box 10940
Pittsburgh, PA 15236-0940

3610 Collins Ferry Road
P.O. Box 880
Morgantown, WV 26507-0880

One West Third Street, Suite 1400
Tulsa, OK 74103-3519

1450 Queen Avenue SW
Albany, OR 97321-2198

2175 University Ave. South
Suite 201
Fairbanks, AK 99709

Visit the NETL website at:
www.netl.doe.gov

Customer Service:
1-800-553-7681